Initial results from the InSight mission on Mars

W. Bruce Banerdt[*1] and Suzanne E. Smrekar[*1], Don Banfield[2], Domenico Giardini[3], Matthew Golombek[1], Catherine L. Johnson[4,5], Philippe Lognonné[6,7], Aymeric Spiga[8], Tilman Spohn[9], Clément Perrin[6], Simon C. Stähler[3], Daniele Antonangeli[10], Sami Asmar[1], Caroline Beghein[11,12], Neil Bowles[13], Ebru Bozdag[14], Peter Chi[11], Ulrich Christensen[15], John Clinton[3], Gareth S. Collins[16], Ingrid Daubar[1], Véronique Dehant[17,18], Mélanie Drilleau[6], Matthew Fillingim[19], William Folkner[1], Raphaël F. Garcia[20], Jim Garvin[21], John Grant[22], Matthias Grott[9], Jerzy Grygorczuk[23], Troy Hudson[1], Jessica C. E. Irving[24], Günter Kargl[25], Taichi Kawamura[6], Sharon Kedar[1], Scott King[26], Brigitte Knapmeyer-Endrun[27], Martin Knapmeyer[9], Mark Lemmon[28], Ralph Lorenz[29], Justin N. Maki[1], Ludovic Margerin[30], Scott M. McLennan[31], Chloe Michaut[32,7], David Mimoun[20], Anna Mittelholz[4], Antoine Mocquet[33], Paul Morgan[14,34], Nils T. Mueller[9], Naomi Murdoch[20], Seiichi Nagihara[35], Claire Newman[36], Francis Nimmo[37], Mark Panning[1], William T. Pike[38], Ana-Catalina Plesa[9], Sébastien Rodriguez[6,7], Jose Antonio Rodriguez-Manfredi[39], Christopher T. Russell[11], Nicholas Schmerr[40], Matt Siegler[5,41], Sabine Stanley[42], Eléanore Stutzmann[6], Nicholas Teanby[43], Jeroen Tromp[24], Martin van Driel[3], Nicholas Warner[44], Renee Weber[45], Mark Wieczorek[46]

Affiliations:

1. Jet Propulsion Laboratory, California Institute of Technology, Pasadena, CA 91109, USA
2. Cornell University, Cornell Center for Astrophysics and Planetary Science, Ithaca, NY 14853, USA
3. Institute of Geophysics, ETH Zurich, Sonneggstr. 5, 8092 Zurich, Switzerland
4. Department of Earth, Ocean and Atmospheric Sciences, University of British Columbia, Vancouver, BC, V6T 1Z4, Canada
5. Planetary Science Institute, Tucson, AZ 85719, USA
6. Université de Paris, Institut de Physique du Globe de Paris, CNRS, F-75005 Paris, France
7. Institut Universitaire de France, 1 rue Descartes, 75005 Paris, France
8. Laboratoire de Météorologie Dynamique/Institut Pierre Simon Laplace (LMD/IPSL), Sorbonne Université, Centre National de la Recherche Scientifique (CNRS), École Polytechnique, École Normale Supérieure (ENS), Campus Pierre et Marie Curie BC99, 4 place Jussieu, 75005 Paris, France
9. German Aerospace Center (DLR), Institute of Planetary Research, Rutherfordstr. 2, 12489 Berlin, Germany
10. Sorbonne Université, Muséum National d'Histoire Naturelle, UMR CNRS 7590, Institut de Minéralogie, de Physique des Matériaux et de Cosmochimie, IMPMC, 75005 Paris, France
11. Department of Earth, Planetary, and Space Sciences, University of California, Los Angeles, 595 Charles Young Drive East, Box 951567, Los Angeles, CA 90095-1567, USA
12. Lunar and Planetary Institute, Universities Space Research Association, 3600 Bay Area Blvd, Houston, TX 77058, USA
13. University of Oxford, Department of Physics, Parks Road, Oxford OX1 3PU, UK
14. Colorado School of Mines, Department of Geophysics, 1500 Illinois Street, Golden, CO 80401, USA
15. Max Planck Institute for Solar System Research, Justus-von-Liebig-Weg 3, 37077 Göttingen, Germany
16. Department of Earth Science and Engineering, Imperial College London, South Kensington Campus, London SW7 2AZ, UK
17. Royal Observatory of Belgium, Directorate "Reference Systems and Planetology", 3 avenue Circulaire, B1180 Brussels, Belgium

18. Université Catholique de Louvain (UCLouvain), Louvain-la-Neuve, Belgium
19. University of California, Berkeley, Space Sciences Laboratory, 7 Gauss Way, Berkeley, CA 94720-7450, USA
20. Institut Supérieur de l'Aéronautique et de l'Espace SUPAERO, 10 Avenue Edouard Belin, 31400 Toulouse, France
21. NASA Goddard Space Flight Center, 8800 Greenbelt Road, Greenbelt, MD 20771, USA
22. Center for Earth and Planetary Studies, National Air and Space Museum, Smithsonian Institution, 6th at Independence Ave. SW, Washington, DC, 20560, USA
23. Astronika Sp. z o.o., ul. Bartycka 18, 00-716 Warszawa, Poland
24. Department of Geosciences, Princeton University, Princeton, NJ, 08544, USA
25. Space Research Institute, Austrian Academy of Sciences (ÖAW), Schmiedlstr. 6, 8042 Graz, Austria
26. Virginia Tech, Department of Geosciences, 926 West Campus Drive, Blacksburg, VA, 24061, USA
27. Bensberg Observatory, University of Cologne, Vinzenz-Pallotti-Str. 26, 51429 Bergisch Gladbach, Germany
28. Space Science Institute, 4765 Walnut Street, Suite B, Boulder, CO 80301, USA
29. Johns Hopkins Applied Physics Laboratory, 11100 Johns Hopkins Road, Laurel, MD 20723, USA
30. Institut de Recherche en Astrophysique et Planétologie, Université Toulouse III Paul Sabatier, CNRS, CNES, 14 Av. E. Belin, 31400, Toulouse, France
31. Department of Geosciences, Stony Brook University, Stony Brook, NY, 11794-2100, USA
32. Université de Lyon, École Normale Supérieure de Lyon, UCBL, CNRS, Laboratoire de Géologie de Lyon -Terre, Planètes, Environnement, 69007 Lyon, France
33. Laboratoire de Planétologie et Géodynamique, UMR6112, Université de Nantes, Université d'Angers, CNRS, 2 rue de la Houssinière - BP 92208, 44322 Nantes Cedex 3, France
34. Colorado Geological Survey, c/o 8149 Ryber Rd, Wilsonville, OR 97070, USA
35. Department of Geosciences, Texas Tech University, Lubbock, Texas 79409 USA
36. Aeolis Research, 333 N Dobson Road, Unit 5, Chandler AZ 85224-4412, USA
37. Department of Earth and Planetary Sciences, University of California Santa Cruz, Santa Cruz, CA 95064, USA
38. Department of Electrical and Electronic Engineering, Imperial College London, South Kensington Campus, London, SW7 2AZ, UK
39. Centro de Astrobiología (CSIC-INTA), 28850 Torrejón de Ardoz, Madrid, Spain
40. University of Maryland, College Park, Department of Geology, 8000 Regents Dr., College Park, MD, 20782-4211, USA
41. Southern Methodist University, Earth Science, 3225 University Blvd, Dallas, TX 75205, USA
42. Johns Hopkins University, 3400 N. Charles St., Baltimore, MD, 21218, USA
43. School of Earth Sciences, University of Bristol, Wills Memorial Building, Queens Road, Bristol BS8 1RJ, UK
44. Department of Geological Sciences, State University of New York at Geneseo, 1 College Circle, Geneseo, NY 14454, USA
45. NASA Marshall Space Flight Center (MSFC), NSSTC Mail Code ST13, 320 Sparkman Drive, Huntsville, AL 35805, USA
46. Université Côte d'Azur, Observatoire de la Côte d'Azur, CNRS, Laboratoire Lagrange, France

NASA's InSight (Interior exploration using Seismic Investigations, Geodesy and Heat Transport) mission landed in Elysium Planitia on Mars on 26 November 2018. It aims to determine the interior structure, composition, and thermal state of Mars, as well as constrain present-day seismicity and impact cratering rates. Such information is key to understanding the differentiation and subsequent thermal evolution of Mars, and thus the forces that shape the planet's surface geology and volatile processes. Here we report an overview of the first

10 months of geophysical observations by InSight. As of 30 September 2019, 174 seismic events have been recorded by the lander's seismometer, including over 20 events of moment magnitude M_{w} 3 to 4. The detections thus far are consistent with tectonic origins, with no impact-induced seismicity yet observed, and indicate a seismically active planet. An assessment of detections suggests that the frequency of global seismic events below approximately M_{w} 3 is similar to that of terrestrial intraplate seismic activity, but there are relatively fewer larger quakes; no quakes exceeding M_{w} 4 have been observed. The lander's other instruments - two cameras, atmospheric pressure, temperature and wind sensors, a magnetometer and a radiometer – have yielded much more than the intended supporting data for seismometer noise characterization: magnetic field measurements indicate a local magnetic field that is ten times stronger than orbital estimates and meteorological measurements reveal a more dynamic atmosphere than expected, hosting baroclinic and gravity waves and convective vortices. With the mission due to last for an entire Martian year or longer, these results will be built upon by further measurements by the InSight lander.

This paper provides a brief mission overview and reports key discoveries to date. We present the first measurement of seismic activity rate, which fundamentally constrains the geological vigor of the planet (note that this study is part of the first set of InSight science reports; two additional papers[1;2] also include interpretation of InSight seismic data[3;4]). The data acquired thus far also enable the characterization of Mars seismic background and upper crust structure, a preliminary analyses of the basic character of seismicity, local geology, atmospheric processes at the surface, and the characteristics of the surface magnetic field[1;2;5–7]. InSight's payload (Extended Data Figure 1) is similar to that deployed on the Moon by Apollo astronauts and consists of three primary investigations: Seismic Experiment for Interior Structure (SEIS)[8]; the Heat Flow and Physical Properties Package (HP^3)[9]; and Rotation and Interior

Structure Experiment (RISE)[10]. These provide a synergistic view of the martian interior, as seismology is most effective in delineating the outer layers of a planet (crust and mantle) whereas determination of the rotational dynamics by RISE is particularly well-suited for probing the properties of the deep core. Heat flow measurements provide insight into the dynamics of the interior, which is complementary to the structural information from SEIS and RISE. HP^3 and RISE have not yet collected sufficient data for meaningful analysis; thus their results will not be discussed here. As originally planned, InSight is expected to require upwards of 24 months ($\sim$1 Mars year) to achieve all of its objectives.

The Auxiliary Payload Sensor Suite (APSS) supports these investigations, including a deployment system (including two cameras) and a set of sensors intended to measure sources of seismic noise (wind, pressure, and magnetic field). A unique aspect of these sensors is that because they were designed to have performance commensurate with SEIS (e.g., the pressure sensor has a sensitivity in the seismic frequency band sufficient to measure variations that can cause ground deformations that appear in the seismic data), they are well-suited for providing diverse simultaneous measurements of phenomena both endogenic and exogenic (see Extended Data Figure 1).

Data are acquired continuously at 100 sps for SEIS and 20 sps for APSS, but only a fraction of this data can be returned due to transmission limitations. High-rate data are stored on the lander for $>$1 month, while sub-sampled continuous data sets for SEIS and APSS are returned daily and evaluated rapidly on the ground by the science team. The science team then submits 'event requests' for the lander to return full-rate data for specific time intervals that contain seismic, atmospheric, or magnetic events of interest.

Upon landing, InSight began immediately acquiring images, followed soon after by APSS,

radiometer, and SEIS Short Period (SP) observations, along with multiple RISE X-band tracking passes each week. The first three weeks were dedicated to choosing the best locations on the ground for placement of the SEIS and HP^3 instruments[5]. Installation of SEIS and its wind shield was completed on sol 70 (a sol is a Martian day). SEIS data was acquired prior to this time (including on the deck), but it did not achieve full performance until completion of its calibration and tuning around sol 85. Currently SEIS is performing significantly better than its design requirements at frequencies between 0.2 and 2 Hz, with a noise floor of $\sim 3\times10^{-9} m/s^2/Hz^{1/2}$ for the SP sensors and slightly above $1\times10^{-10} m/s^2/Hz^{1/2}$ for the very broad band (VBB) sensors during the early evening when the atmosphere is still[1].

Geologic Context and Shallow Structure of the Regolith

InSight landed in western Elysium Planitia (4.502°N, 135.623°E, elevation -2.613 km; see Figure 1), a volcanic plain with surface ages ranging from 3.7 Gy to 2.5 My[5]. Cerberus Fossae, approximately 1600 km to the east, contains faults, volcanic flows and liquid water outflow channels with ages as recent as 2-10 My and possibly younger from impact crater counts[11;12]. The lander sits in a ~25 m diameter degraded impact crater, informally named Homestead hollow, filled with impact-generated sediments that have been transported and modified by wind. The local depth to a rocky layer inferred to be ancient lava flows is approximately 3-5 m based on the depth at which nearby impacts have excavated boulders[13;14].

Coordinated synergistic observations by InSight's instruments are providing new ways of characterizing the near-subsurface of Mars. The seismic recording of the HP^3 hammer strokes[15] and of seismic signals due to atmospheric vortices[16;17] sound the first few meters of the subsurface adjacent to the lander, confirming a high-porosity, low-rigidity layer ~3 meters thick, above a much more rigid layer[1]. Independently, a unique joint observation of a dust devil vortex using orbital imaging with the lander's cameras, pressure sensor and

seismometer yielded a measurement of Young's modulus of 270 MPa in the upper few meters (see Box and Supplementary Discussion). This value, which is localized at a distance of ∼20 m from the lander, is larger than that immediately adjacent to the lander. This is consistent with the latter having an upper layer of relatively unconsolidated eolian material which filled Homestead hollow after its formation. Finally, the infrared radiometer has measured the thermal inertia of the near-surface[5] to be 160-230 $J/m^2/s^{1/2}/K^1$, consistent with expectations of a poorly-consolidated, sandy surface layer[13;18].

Atmospheric and Magnetic Measurements

Although in-situ meteorological measurements have been made previously, InSight's continuous and simultaneous, well-calibrated, high-rate, high-precision pressure, wind and air temperature data provide an unprecedented view of Mars' surface environment. The characteristics of the bulk atmosphere and boundary layer phenomena are sampled on time scales of seconds to months[6;19] (Figure 2). And, as discussed above, the sensitivity of SEIS to both wind- and pressure-induced signals[1;17;20–24] make it a unique complementary meteorological sensor for short-time-scale phenomena.

The InSight landing site exhibits strong daytime turbulence, being the most active site among previous and current landed missions to date for dust devil-like vortices. The pattern of turbulence and calm is strongly periodic, repeating daily over the time span thus far observed. This pattern defines the low-noise windows for SEIS marsquake observations[1;2]. Conversely, the dynamic atmosphere provides vibrational and ground tilt signals that can be used both to help characterize the meteorological phenomena and to probe the mechanical structure of the upper few meters of the regolith (see Lognonné et al.[1] and Supplementary Discussion). On synoptic scales, InSight detects surprisingly large signals from mid-latitude baroclinic waves (with periods of 2-7 sols, similar to those detected by previous landers and from orbit), in

addition to the expected diurnally repeating solar-driven pressure variations from thermal tides and the longer timescale signature of CO_2 seasonal condensation (which matches in shape that measured from prior landers). A few months after landing a regional storm changed the weather at the InSight landing site, with wind direction shifting diametrically. Other mesoscale phenomena include gravity waves (regular oscillations in pressure, wind or air temperature driven by buoyancy oscillations and with periods >100 s), which are more ubiquitous than previously thought, and the first detections of bore events (soliton-like waves) and infrasound on Mars[24]. All of these phenomena are interesting from an atmospheric science perspective, but also must be well-understood to properly isolate atmospheric effects from true seismic sources.

The InSight Fluxgate magnetometer (IFG) is one of the auxiliary instruments that monitor environmental conditions for the SEIS experiment. It is also the first magnetometer on the surface of Mars and allows studies of static and time-varying magnetic fields (Figure 3). Although the lander itself produces both such fields, signals of Martian origin can contribute to understanding the atmosphere and ionosphere regionally, as well as the interior structure of Mars. Joint studies of InSight and MAVEN (Mars Atmosphere and Volatile Evolution mission) magnetic field data, using new observations from the MAVEN spacecraft above InSight, will provide unique opportunities for studying how external fields measured in and above the ionosphere are manifest on the ground.

Satellite missions have measured crustal magnetization acquired in an ancient global field[25]. However, only surface measurements can identify weak and/or small-scale magnetizations that provide key constraints on crustal structure. The static crustal field measured by InSight has a strength of 2013 ±53 nT, and points south-east and upward. The field strength exceeds predicted surface fields at this location from combined MAVEN and MGS (Mars Global Surveyor) satellite measurements by an order of magnitude[26–28] and hence implies

locally strong magnetization with wavelengths less than ∼150 km. Furthermore, the inferred magnetization is consistent with an Earth-like ancient dynamo field and is probably carried within a layer at least 3.9 Ga old[7].

So far, time-varying signals that have been confidently detected are diurnal variations and shorter period pulsations (100-1000 s). Peak-to-peak amplitudes of diurnal variations are ∼20 nT and exceed those expected from the interplanetary magnetic field alone, indicating contributions from ionospheric currents. IFG has also detected transient signals possibly related to atmospheric or space weather. With a longer time-series, we expect to find signals with seasonal and/or annual variations and 26-sol cyclicity that results from solar rotations and the resulting periodic changes in the interplanetary field at Mars. More details are provided in Johnson et al.[7].

The time-varying magnetic fields are key to future studies of electrical conductivity structure, acting as a probe of interior temperature, mineralogy and volatile content. The crustal magnetization and future electrical conductivity sounding therefore contribute directly to the overarching mission science goals.

Seismic Activity of Mars

The InSight marsquake catalog (through 30 September 2019) contains 174 events[2;4], 150 of which have a high-frequency character (with significant energy only above ∼1 Hz) and are not yet fully understood in terms of distance and magnitude. The other 24 have dominantly low-frequency content, and their spectral shapes follow the same scaling laws as earthquakes and moonquakes, leading us to conclude that they are of tectonic origin[2]. The character of these spectra are compatible with expectations for distant tectonic events, and three of these have sufficiently high signal-to-noise ratio (SNR) to be clearly located. Assuming similar

signatures between these three events and another ten with lower SNR, rough distances and moment magnitudes can be computed for 13 events (see Extended Data Figure 3 and Table 1 in Giardini et al.[2]). At least two of these events are located in the Cerberus Fossae region, consistent with the interpretation from orbital imaging of an active volcano-tectonic system.

Figure 4 shows two examples of these low-frequency marsquake signals compared to two terrestrial events at similar distances from the receivers. S0235b has clearly defined P- and S-wave arrivals. The time difference between these arrivals along with their measured polarization allows location of the epicenter of the quake and determination of its moment magnitude. P and S arrivals for lower SNR signals such as S0105a are difficult to pick from simple inspection of the time series, and are estimated using spectral density envelopes (see Giardini et al.[2] for details). Compared to terrestrial quakes, marsquakes show relatively long codas after each seismic arrival, indicative of strong scattering in the crust, and lack surface waves. Whether the latter is due to deep sources, crustal scattering, or other reasons is yet unknown.

Meteoroid impacts are an additional expected source of seismic events, and can be used to both probe the crust and constrain the impact flux. In theory, factors such as the direction of first motion, the occurrence of surface waves or depth phases, the amplitude ratio of P/S waves, and frequency spectrum can all be used to discriminate between impacts and endogenic sources[29]. Impact detections of up to 10 per Earth year were predicted[29]. Using the measured ambient seismic noise[1], the updated predicted annual detection rate is $\sim$8 (0.1-200) for the SEIS VBB and $\sim$2 (0.02-20) for the SEIS SP[30;31]. All estimates have roughly an order of magnitude uncertainty due to factors such as unknown impact-seismic efficiency, attenuation and scattering in the martian interior.

No impacts have been unequivocally identified to date, possibly due to the scattering[1] that can obscure surface waves and depth phases[2]. Thus we cannot definitively rule out an impact origin for any particular event. However the similarity of observed waveforms points to a common seismic origin[2]. To actively guide the search for candidate events in the seismic record, orbital images are being analyzed for new albedo features characteristic of recent impacts. InSight has also begun using its cameras for night time imaging to search for meteors. None have yet been identified[31].

The level of seismic activity is crucial for investigating interior structure and understanding Mars' thermal and chemical evolution. Martian seismicity predictions are based on evidence of faulting[32;33] and thermal evolution models that directly link seismicity to lithospheric cooling[34–36]. Prior to InSight, the only direct constraint was the absence of unambiguous event detections by the Viking 2 seismometer[37;38]. This restricted activity to be lower than a few percent of global terrestrial seismic activity.

Accounting for possible events that may be masked at noisier times and using source-spectral scaling to estimate magnitudes (see detailed analysis in Giardini et al.[2]), we determine magnitude- and distance-dependent detectability statistics and estimate the total annual seismic activity using the 13 confirmed events. We extrapolate the number of observed events to (i) one full year, assuming statistical stationarity of the seismicity release, (ii) to the full sol, taking into account the observed, highly variable noise profile, and finally (iii) to the full planet, accounting for the detectability of events of different magnitudes with distance (see Methods). For example, the handful of events with M_{w} 3.0-3.2 are the detectable fraction of an estimated several tens to a hundred events per Earth year across the planet.

Our estimated global seismic event rate derived from observed events (Figure 5) indicates a moderately active planet, with a value far above that of the Moon (excluding deep moonquakes, which are associated with tidal stresses)[39] and slightly below intraplate Earth[46]. We note that the activity is relatively close to the initial predictions[32] that were used to guide performance requirements and is within the uncertainty estimates of Knapmeyer et al.[35].

Another robust observation is the absence of events above $M_{\mathrm{w}} \geq 4$. Compared to the Gutenberg-Richter magnitude distribution with $b \sim 1$ commonly observed on the Earth and the Moon (where b is the logarithmic slope of the cumulative magnitude-number curve; see Figure 5), the current distribution of events appears to be skewed to smaller events ($b > 1$). On Earth higher b values are only observed in specific tectonic settings, such as extensional areas[40] or extremely low-strain-rate oceanic intraplate regions[41], as well as locally in volcanic areas. We note that the robust determination of b requires much larger datasets[42] and will only be possible later in the mission. To connect the seismicity to geodynamic modelling and the global heat budget[36] requires an estimate of the full planetary moment release, which is dominated by the largest events in the distribution[43], at least for b near 1.

First results from the InSight seismometer are beginning to unveil Mars' interior structure, rate of seismicity, and locations of current tectonic activity. Observations by other instruments reveal high crustal magnetization and unexpected atmospheric processes, such as high levels of vortex activity and strong mid-latitude baroclinic waves. With more than another year of planned observations, InSight's focus on interior processes utilizing its diverse suite of highly complementary instruments is expected to refine the rate and distribution of seismic activity and delineate the thickness of the crust, the size and density of the core, and bound the planetary heat flow. These observations should continue to lead to new discoveries and constraints on Mars' interior structure and geologic evolution, and processes of planetary differentiation and thermal evolution.

Box Text

Box. Subsurface Structure from Multi-Instrument Observations of Vortices.

Through multi-instrument observations of the same phenomena, the InSight mission provides unique opportunities both to better understand atmospheric processes and to investigate the sub-surface structure of Mars. An example of this is the first joint observations of a dust devil vortex on a planetary surface made by both orbital imaging and a suite of in-situ instruments. From differences between sequential wide-angle Instrument Context Camera (ICC) images we are able to identify a track left by a vortex and establish its time of passage, allowing the isolation of this particular event in the pressure, wind and seismic data. Using the observed time of passage, we identified the same track in High Resolution Imaging Science Experiment (HiRISE) images from the Mars Reconnaissance Orbiter, which gave the precise two-dimensional trajectory of the dust devil. By combining this information we can make detailed measurements of the compliance of the Martian subsurface in a specific known location. In addition, whereas dust devil vortex parameters (diameter, core pressure drop) can normally only be determined if the vortex passes directly over the meteorological instrumentation, these synergetic measurements allow us to remotely access the properties of the vortex without the need for a direct encounter.

Our observations allow us to use the deformation by the negative pressure load of the vortex to derive the compliance, or elastic rigidity, of the ground near the InSight lander. This is a key parameter in characterizing the mechanical properties of the martian subsurface and understanding surface formation and modification processes on Mars. As detailed in the Supplementary Discussion, we derive a mean Young's modulus of around 270 MPa, increasing with depth, for an area roughly 20 m WSW of the lander. This value is larger than that found by Lognonné et al.[1] using the seismic shear velocity V_s (measured next to the lander from the HP^3 hammer strokes) to constrain the result from modeling several

hundred non-located vortices. This suggests that the regolith 15-25 meters from InSight is more rigid than the material immediately adjacent to the lander beneath SEIS and HP^3, which is consistent with the latter having an upper layer of relatively unconsolidated eolian material which filled Homestead hollow after its formation.

References

[1] Lognonné, P., et al. Constraints on the shallow elastic and anelastic structure of Mars from InSight seismic data. *Nat. Geosci.* https://doi.org/10.1038/s41561-020-0536-y (2020).

[2] Giardini, D., et al. The seismicity of Mars. *Nat. Geosci.* https://doi.org/10.1038/s41561-020-0539-8 (2020).

[3] InSight Mars SEIS data Service et al. SEIS raw data, InSight Mission. *Other/Seismic Network* https://doi.org/10.18715/SEIS.INSIGHT.XB_2016 (2019).

[4] InSight Marsquake Service et al. Mars Seismic Catalogue, InSight Mission; V1 2/1/2020. *Dataset* https://doi.org/10.12686/a6 (2020).

[5] Golombek, M., et al. Geology of the InSight landing site, Mars. *Nat. Commun.* https://doi.org/10.1130/abs/2019am-336461 (2020).

[6] Banfield, D., & Spiga, A., et al. The atmosphere of Mars as observed by InSight. *Nat. Geosci.*, in press (2020).

[7] Johnson, C. L., et al. Crustal and time-varying magnetic fields at the InSight landing site on Mars. *Nat. Geosci.*, in press (2020).

[8] Lognonné, P., et al. SEIS: InSight's seismic experiment for internal structure of Mars. *Space Sci. Rev.*, **215** https://doi.org/10.1007/s11214-018-0574-6 (2019).

[9] Spohn, T., et al. The Heat Flow and Physical Properties Package (HP^3) for the InSight mission. *Space Sci. Rev.*, **214** https://doi.org/10.1007/s11214-018-0531-4 (2018).

[10] Folkner, W. M., et al. The Rotation and Interior Structure Experiment on the InSight mission to Mars. *Space Sci. Rev.*, **214** https://doi.org/10.1007/s11214-018-0530-5 (2018).

[11] Vaucher, J., et al. The volcanic history of central Elysium Planitia: Implications for Martian magmatism. *Icarus*, **204**, 418–442 (2009).

[12] Burr, D. M., Grier, J. A., McEwen, A. S., and Keszthelyi, L. P. Repeated aqueous flooding from the Cerberus Fossae: Evidence for very recently extant, deep groundwater on Mars. *Icarus*, **159**, 53–73 (2002).

[13] Golombek, M. P., et al. Selection of the InSight landing site. *Space Sci. Rev.*, **211**, 5–95 (2017).

[14] Golombek, M. P., et al. Geology and physical properties investigations by the InSight lander. *Space Sci. Rev.*, **214** https://doi.org/10.1007/s11214-018-0512-7 (2018).

[15] Kedar, S., et al. Analysis of regolith properties using seismic signals generated by InSight's HP^3 penetrator. *Space Sci. Rev.*, **211**, 315–337 (2017).

[16] Lorenz, R. D., et al. Seismometer detection of dust devil vortices by ground tilt. *Bull. Seismol. Soc. Am.*, **105**, 3015–3023 (2015).

[17] Kenda, B., et al. Modeling of ground deformation and shallow surface waves generated by martian dust devils and perspectives for near-surface structure inversion. *Space Sci. Rev.*, **211**, 501–524 (2017).

[18] Morgan, P., et al. A pre-landing assessment of regolith properties at the InSight landing site. *Space Sci. Rev.*, **214** https://doi.org/10.1007/s11214-018-0537-y (2018).

[19] Spiga, A., et al. Atmospheric science with InSight. *Space Sci. Rev.*, **214** https://doi.org/10.1007/s11214-018-0543-0 (2018).

[20] Teanby, N. A., et al. Seismic coupling of short-period wind noise through Mars' regolith for NASA's InSight lander. *Space Sci. Rev.*, **211**, 485–500 (2017).

[21] Mimoun, D., et al. The noise model of the SEIS seismometer of the InSight mission to Mars. *Space Sci. Rev.*, **211**, 383–428 (2017).

[22] Murdoch, N., et al. Evaluating the wind-induced mechanical noise on the InSight seismometers. *Space Sci. Rev.*, **211**, 429–455 (2017).

[23] Murdoch, N.. Alazard, D., Knapmeyer-Endrun, B., Teanby, N. A., Myhill, R. Flexible mode modelling of the InSight lander and consequences for the SEIS instrument. *Space Sci. Rev.*, **214** https://doi.org/10.1007/s11214-018-0553-y (2018).

[24] Banfield, D., et al. InSight Auxiliary Payload Sensor Suite (APSS). *Space Sci. Rev.*, **215** https://doi.org/10.1007/s11214-018-0570-x (2019).

[25] Acuña, M. H., et al. Global distribution of crustal magnetization discovered by the Mars Global Surveyor MAG/ER experiment. *Science*, **284**, 790–793 (1999).

[26] Mittelholz, A., Johnson, C. L., & Morschhauser, A. A new magnetic field activity proxy for Mars from MAVEN data. *Geophys. Res. Lett.*, **45** 5899–5907 (2018).

[27] Smrekar, S. E., et al. Pre-mission InSights on the interior of Mars. *Space Sci. Rev.*, **215** https://doi.org/10.1007/s11214-018-0563-9 (2019).

[28] Langlais, B., Thébault, E., Houliez, A., Purucker, M. E., & Lillis, R. J. A new model of the crustal magnetic field of Mars using MGS and MAVEN. *J. Geophys. Res. Planets*, **124**, 1542–1569 (2019).

[29] Daubar, I., et al. Impact-seismic investigations of the InSight mission. *Space Sci. Rev.*, **214** https://doi.org/10.1007/s11214-018-0562-x (2018).

[30] Teanby, N. A., et al. Impact detection with InSight: Updated estimates using measured seismic noise on Mars. *Lunar Planet. Sci.*, **50**, abstract #1565 (2019).

[31] Daubar, I. J., et al. Impact science on the InSight mission – current status. *Int. Conf. Mars*, **9**, abstract #6198 (2019).

[32] Golombek, M. P., Banerdt, W. B., Tanaka, K. L., & Tralli, D. M. A prediction of Mars seismicity from surface faulting. *Science*, **258**, 979–981 (1992).

[33] Golombek, M. P. A revision of Mars seismicity from surface faulting. *Lunar Planet. Sci.*, **43**, abstract #1244 (2002).

[34] Phillips, R. J., & Grimm, R. E. Martian seismicity. *Lunar Planet. Sci.*, **22**, abstract #1061 (1991).

[35] Knapmeyer, M., et al. Working models for spatial distribution and level of Mars' seismicity. *J. Geophys. Res. Planets*, **111** https://doi.org/10.1029/2006JE002708 (2006).

[36] Plesa, A. C., et al. Present-day Mars' seismicity predicted from 3-D thermal evolution models of interior dynamics. *Geophys. Res. Lett.*, **45**, 2580–2589 (2018).

[37] Anderson, D. L., et al. Seismology on Mars. *J. Geophys. Res.*, **82**, 4524–4546 (1977).

[38] Goins, N. R., & Lazarewicz, A. R. Martian seismicity. *Geophys. Res. Lett.*, **6**, 368–370 (1979).

[39] Oberst, J. Unusually high stress drops associated with shallow moonquakes. *J. Geophys. Res.*, **92** (B2), 1397–1405 (1987).

[40] Petruccelli, A., et al. The influence of faulting style on the size-distribution of global earthquakes. *Earth Planet Sc. Lett.*, **527** https://doi.org/10.1016/j.epsl.2019.115791 (2019).

[41] Sasajima, R., & Ito, T. Strain rate dependency of oceanic intraplate earthquake b-values at extremely low strain rates. *J. Geophys. Res. Solid Earth*, **121**, 4523–4537 (2016).

[42] Marzocchi, W., & Sandri, L. A review and new insights on the estimation of the b-value and its uncertainty. *Ann. Geophys.*, **46**, 1271–1282 (2003).

[43] Knapmeyer, M., et al. Estimation of the seismic moment rate from an incomplete seismicity catalog, in the context of the InSight mission to Mars. *Bull. Seismol. Soc. Am.*, **109**, 1125–1147 (2019).

[44] Swiss Seismological Service (SED). National Seismic Networks of Switzerland. https://doi.org/10.12686/sed/networks/ch (1983).

[45] Smith, D. E., et al. Mars Orbiter Laser Altimeter: Experiment summary after the first year of global mapping of Mars. *J. Geophys. Res. Planets*. **106**, 23689–23722 (2001).

[46] Okal, E. A., & Sweet, J. R. Frequency-size distributions for intraplate earthquakes. *Geol. Soc. Am. Bull.* **425**, 59–71 (2007).

Correspondence and requests for materials should be addressed to Bruce Banerdt (william.b.banerdt@jpl.nasa.gov) or Suzanne Smrekar (suzanne.e.smrekar@jpl.nasa.gov).

Acknowledgements

A portion of the work was supported by the InSight Project at the Jet Propulsion Laboratory (JPL), California Institute of Technology, under a contract with the National Aeronautics and Space Administration (NASA). We acknowledge NASA; CNES (Centre Nationale d'Etudes Spatiale); their partner agencies and Institutions UKSA (United Kingdom

Space Agency), SSO (Swiss Space Office), DLR (Deutsches Zentrum für Luft- und Raumfahrt), JPL, IPGP-CNRS (Institute de Physique du Globe de Paris-Centre National de la Recherche Scientifique), ETHZ (Eidgenössische Technische Hochschule Zürich), IC (Imperial College), MPS-MPG (Max Planck Institute for Solar System Research-Max Planck Gesellschaft); INTA/CSIC-CAB (Instituto Nacional de Técnica Aeroespacial/Consejo Superior de Investigaciones Científicas-Centro Astrobioligía); and the flight operations team at JPL, SISMOC (SEIS on Mars Operations Center), MSDS (Mars SEIS Data Service), IRIS-DMC (Incorporated Research Institutions for Seismology-Data Management Center) and PDS n(planetary Data Service) for providing the SEED (Standard for the Exchange of Earthquake Data) SEIS data used in the seismicity analysis. French co-authors acknowledge the French Space Agency CNES, CNRS and ANR (Agence Nationale pour la Recherche) (ANR-10-LABX-0023, ANR-11-IDEX-0005-0). The Swiss co-authors were jointly funded by the Swiss National Science Foundation (SNF-ANR project 157133), the Swiss State Secretariat for Education, Research and Innovation (SEFRI project "MarsQuake Service-Preparatory Phase") and ETH Research grant ETH-06 17-02. This is InSight Contribution Number 100.

Author contributions

The scientific results of the InSight mission are the result of a team effort, with all the listed authors contributing to aspects of the design, implementation and analysis of results. W.B.B. and S.E.S. are Principal Investigator and Deputy Principal Investigator, respectively, of the InSight mission, and jointly and equally supervised and participated in the work described in the manuscript, as well as contributed substantially to writing the manuscript. P.L., along with D.G. and W.T.P., co-led the design and implementation of the SEIS experiment. The following people contributed to the design and implementation of SEIS: U.C., D.M. and J.T.; and contributed to seismic data analysis: C.B., E.B., J.C., J.I., S. Kedar, B.K.E.,

M.K., L.M., A. Mocquet, F.N., M.P., A.C.P., M.P., N.S. and R.W.. P.L and W.T.P. led the SEIS performance testing, assisted by M.D, B.K.E, R.F.G., S.K., T.K., D.M., and N.M.. D.B. and A.S. co-led the atmospheric science investigation and contributed to writing the manuscript, with N.B., M.L. and C.N. providing input. J.A.R.M. contributed to the design, implementation and analysis of the atmospheric science investigation. R.G. and R.L. contributed to the joint interpretation of the seismic and atmospheric science investigations. J.M. led the imaging experiment and contributed to interpretation of results. M. Golombek led the geology investigation and contributed to writing the manuscript, with J. Garvin, J. Grant, S.R. and N.W. providing input. C.J. and C.T.R. co-led the magnetic investigation and contributed to writing the manuscript, with input from P.C., M.F. and A. Mittelholz. I.D. led the impact cratering investigation, interpretation of results, and write-up for this manuscript, with G.C. and N.T. providing contributions. V.D. and W.F. co-led the geodesy investigation and contributed to interpretation of results, with S.A. providing contributions. T.S. led the heat flow investigation and contributed to writing the manuscript. M. Grott, J. Grygorczuk, T.H., G.K., P.M., N. Müller, S.N., M.S. and S.E.S. contributed to the design, implementation and analysis of the heat flow investigation. C.P. led the analysis and the writing of the regolith properties from ground deformation described in the Supplementary Discussion, with N. Murdoch, M.D., S.R., M.L., E.S., T.K., P.L., A.S. and D.B. providing contributions. S. Stähler led the analysis and writing of the seismic activity estimate described in Methods, with M.K., M.vD. and D.G. providing contributions. D.A., S. King, S.McL., C.M., S. Stanley and M.W. contributed to the interpretation of the planetary interior results.

Competing interests

The authors declare no competing interests.

Figure Captions

Figure 1. Context Map.

InSight (shown as a star) landed on an ancient volcanic plain south of Elysium Mons and north of the martian hemispheric dichotomy. The locations of the Curiosity and Spirit rovers, and the Viking 2 lander, along with major geologic features are shown on a topographic map[45].

Figure 2. The InSight weather station's continuous high-frequency coverage monitors the atmospheric activity from large-scale weather to small-scale turbulence.

The first 200 sols reveal seasonal processes (polar cap CO_2 condensation/sublimation, dust storm), daily variations (baroclinic waves), diurnal variability (thermal tides), mesoscale phenomena (gravity waves, bores), turbulence (dust-devil-like convective vortices) and infrasound.

Figure 3. Multiple phenomena contribute to the magnetic field measured by the IFG.

Time-varying fields (orange) can be of external origin, including the interplanetary magnetic field, ionospheric currents and weather events such as dust devils; they can also be of lander origin (blue), e.g., due to movement of the robotic arm, RISE or UHF communications, solar array currents, or temperature variations causing deformation of the lander. The martian static crustal field (red) results from crustal magnetization, represented schematically here as subsurface dipoles. A DC field is also associated with the lander itself (green). Inset shows IFG (white cube, about 8 cm across) mounted under lander deck).

Figure 4. Marsquakes have similarities and differences with earthquakes.

The upper frame shows vertical displacement times series for two marsquake signals (brown). S0235b is one of the highest SNR thus far observed and shows clear P-wave and S-wave arrivals. S0105a is an example of a lower SNR event; for such events P and S arrivals are determined using power density function envelopes[2]. Note the different amplitude scales. The lower frame shows the vertical components of two earthquake signals at a similar distance, recorded at stations FIESA and DAVOX of the Swiss Seismic Network[44]. The shallow earthquake in Greece has visible surface waves, which are not visible for either the deep earthquake or the marsquakes. All waveforms were corrected for instrument response and filtered between 2 and 8 second period (marsquakes) or 2 and 30 seconds (earthquakes). For the marsquakes, the instrument noise exceeds the signal at about 10 second period, hence the different filter.

Figure 5. Cumulative annual activity rate for Mars compared to Earth, the Moon and pre-mission predictions for Mars.

The brown curve shows the observed number of marsquakes as a function of magnitude from Giardini et al.[2]. The orange curve represents these data extrapolated to the entire planet, with the vertical spread of values representing the uncertainty in the completeness of observation for smaller distant events. The pre-InSight estimate of Mars seismic activity is from Golombek et al.[32]. Lunar seismicity is based on the analysis of shallow moonquake activity by Oberst[39], with the grey area representing the unknown completeness. The global seismicity of the Earth (dark blue line) is from the GlobalCMT catalogue, and is dominated by plate boundaries. The intraplate seismicity estimates separate tectonically deformed regions away from plate boundaries (blue) and stable continental interiors (green)[46]. Terrestrial curves and the upper part of the lunar bar are scaled to the surface area of Mars.

Box Figure. Multiple observations of the effects of an atmospheric vortex (dust devil).

(A) Difference between HiRISE images ESP060695_1845 (July 8, 2019; sol 218) and ESP059495_1845 (April 6, 2019; sol 127) showing new dust devil tracks (dark traces) near the InSight lander. The three main tracks have been highlighted by colored arrows. (B) Difference between ICC images taken on sols 202 and 201. A faint dark dust devil trace is highlighted by yellow arrows. (C) Model data (red) demonstrating one example fit to the observed pressure and seismic data (black) for the vortex that formed track 1. Model parameters for this case are: closest approach distance 19 m; vortex translational speed 9.5 m/s; core pressure drop 5.5 Pa; vortex diameter 6 m; Young's modulus 2.7x108 Pa. See Supplementary Discussion for details.

Data availability

The data shown in the plots within this paper and other findings of this study are available from the corresponding author upon reasonable request. The InSight Mission raw and calibrated data sets are available via NASA's Planetary Data System (PDS). Data are delivered to the PDS according to the InSight Data Management Plan available in the InSight PDS archive. All data sets can be accessed at https://pds-geosciences.wustl.edu/missions/insight/index.html. The InSight seismic event catalogue[4] and waveform data[3] are available from the IRIS-DMC and SEIS-InSight data portal (https://www.seis-insight.eu/en/science). The catalogue and waveform data have the identifiers http://doi.org/10.12686/a6 and https://doi.org/10.18715/SEIS.INSIGHT.XB_2016, respectively. Seismic waveforms as well as data from all other InSight instruments and MOLA topographic data are available from NASA PDS (https://pds.nasa.gov/). The data of terrestrial stations CH.DAVOX and CH.FIESA are part of the Swiss Seismic Network[44]. These data are accessible from the Incorporated Research Institutes for Seismology (IRIS) at https://www.iris.edu/hq/.

Methods

Estimating seismic activity rate from event statistics

The InSight Marsquake Service[47] has detected 174 seismic events, including 13 higher-quality regional and teleseismic (low-frequency or broadband) events (as of September 30, 2019). These latter events were all detected during the quiet evening period and all but one (S0167a) has been determined to be closer than about 90 degrees (one degree equals about 60 km on Mars). To estimate the full seismic activity on Mars, we use only these events. The so-called high-frequency events are of considerably smaller magnitude; their distances are probably $<$500 km, but with large uncertainies[2]. They therefore relate to local seismicity that would not be detected over larger distances and is not necessarily representative of the global seismic activity.

From the environmental noise evolution between 0.1 and 0.8 Hz from sols 85-325, and the modelling of source spectra described by Giardini et al.[2], the fraction of observation time during which an event of a given magnitude and distance would have been observable has been estimated (Extended Data Figure 2). We use these detectability statistics to estimate the total annual seismic activity of Mars from the 13 observed events. These 13 events form **rate A** of our estimate. Extrapolation to full seismicity is done in three steps:

1. **Extrapolation to one year.**

   The events were detected during 231 sols of high quality operations (between sols 85 and 325). Under the assumption of seasonal temporal stationarity, we estimate the annual (with respect to Earth years) activity by multiplying the number of events by 365/231. This results in **rate B**.

2. **Extrapolation to full sol.**

   The ambient noise of Mars varies widely over the course of a sol and none of the events

could have been detected during the noisy, turbulent wind periods of late morning and early afternoon. Therefore, each event is counted n_i=$1/p_i$ times, where p_i is the ratio of time in which an event with its magnitude would have been detectable at a reference distance of 90 degree (see Extended Data Figure 2). This factor n_i varies between 4 for the lowest magnitude ($M_W = 2.8$) and 2 for the highest ones ($M_W = 3.8$); see Extended Data Figure 3. This assumes the events are stationary in time over the duration of one sol. The result is an estimate of the set of events that would have been observed if the noise was at its quietest over the whole mission. In total, it increases the number of events by ~ 3, resulting in **rate C**.

3. **Extrapolation to full planet.**

   The most distant event is a magnitude 3.8 event at an epicentral distance of about 150 degrees, and is about 10 dB above ambient noise. We therefore conclude that the lowest magnitude that can be detected on the whole planet is about 3.5, under best noise conditions. For smaller distances, a threshold magnitude has been estimated from Extended Data Figure 2. This means that, for example, only on 25% of the surface of the planet could magnitude 3.1 events have been detected. Assuming homogeneous distribution of events over the surface of Mars, 75% of the magnitude 3.1 events would therefore remain undetected, even in the quietest periods of the sol. We therefore divide the number of events in each magnitude bin by the fraction of the surface of the planet corresponding to that bin (Extended Data Figure 4), resulting, for example in a factor of 4 for the bin around M_{w}=3.0.

   This results in **rate D**. Since this process is highly sensitive to the minimum magnitude for each distance, it is repeated with $M_{\mathrm{min}} \pm 0.2$ to estimate uncertainties, giving the orange bars in Extended Data Figure 5. This result is shown as the orange range in Figure 5.

Together, the three extrapolation steps result in an estimated annual rate of 100-500 seismic events above M_{w}=2.9. This number is at the upper end of pre-mission predictions[33;35] and almost 100× higher than shallow lunar seismicity[39]. Comparisons to terrestrial seismicity require us to take the lack of martian plate boundaries into account. Global catalogues find about 0.5% of the quakes (M_w>4.5) on Earth in truly intraplate settings (i.e., in non-deformed continental interiors[46]). This assumption has been previously used for estimating the number of observable events expected for InSight[48], but it was not always scaled to the smaller surface area of Mars. The estimate of Martian total seismicity presented here is 25-100% of this "terrestrial, intraplate" value for magnitudes <3. At the same time, marsquakes of magnitudes >3.2 are significantly underrepresented in our current catalog compared to a Gutenberg-Richter distribution with a logarithmic slope b=1.

We recognize that there are different possible scenarios for the distribution of seismic activity on Mars. For example, the Tharsis area may be more active than the southern highlands[36]. If we happen to be preferentially observing a more active region that is relatively close, our estimate of global activity will be biased high. Similarly, if there are active regions that we cannot observe due to distance or obscuration by a seismic shadow zone, our estimate will be low. For now we make the simplest assumption of uniform activity.

Additional References

[47] Clinton, J., et al. The Marsquake Service: Securing daily analysis of SEIS data and building the martian seismicity catalogue for InSight. *Space Sci. Rev.*, **214** https://doi.org/10.1007/s11214–018–0567–5 (2018).

[48] Panning, M. P., et al. Verifying single-station seismic approaches using Earth-based data: Preparation for data return from the InSight mission to Mars. *Icarus*, **527**, 230–242

(2015).

[49] Trebi-Ollennu, A., et al. InSight Mars lander robotics instrument deployment system. *Space Sci. Rev.*, **214** https://doi:10.1007/s11214-018-0520-7 (2018).

[50] Maki, J. N., et al. The color cameras on the InSight lander. *Space Sci. Rev.*, **214** https://doi.org/10.1007/s11214-018-0536-z (2018).

[51] Dell'Agnello, S., et al. LaRRI: Laser Retro-Reflector for InSight Mars lander. *Space Res. Today*, **200**, 25–32 (2017).

Figures

Figure 1.

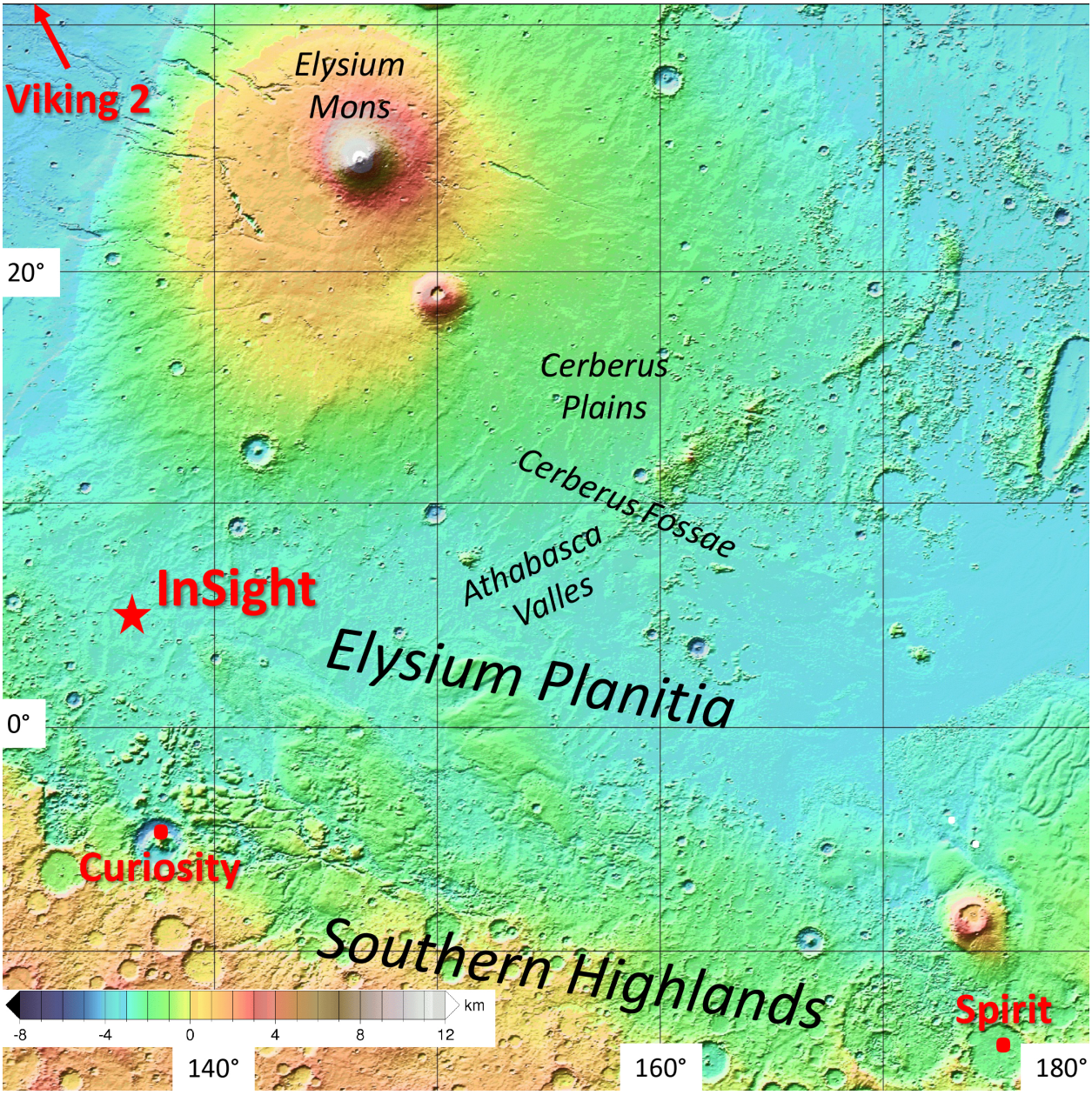

Figure 2.

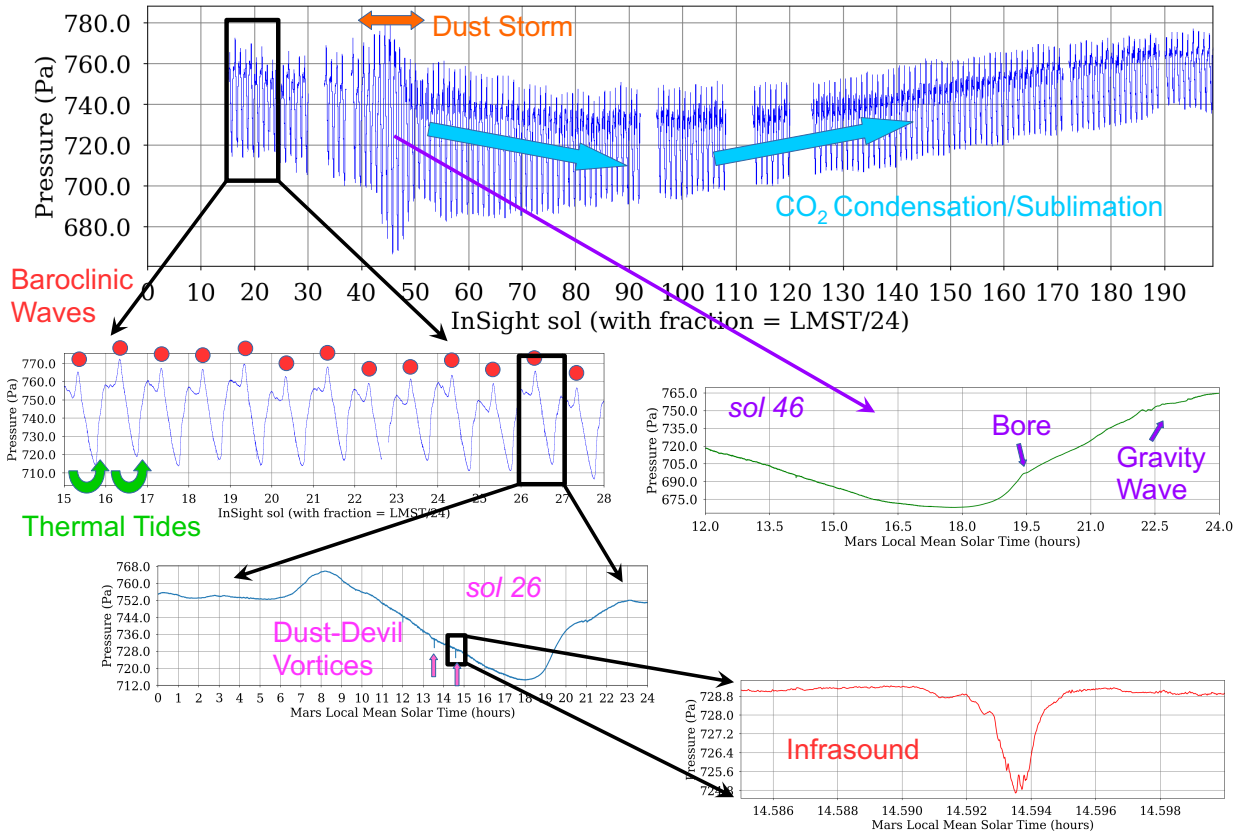
Dust Storm
CO_2 Condensation/Sublimation
Pressure (Pa)
InSight sol (with fraction = LMST/24)
Baroclinic Waves
Thermal Tides
sol 46
Bore
Gravity Wave
Mars Local Mean Solar Time (hours)
sol 26
Dust-Devil Vortices
Infrasound

Figure 3.

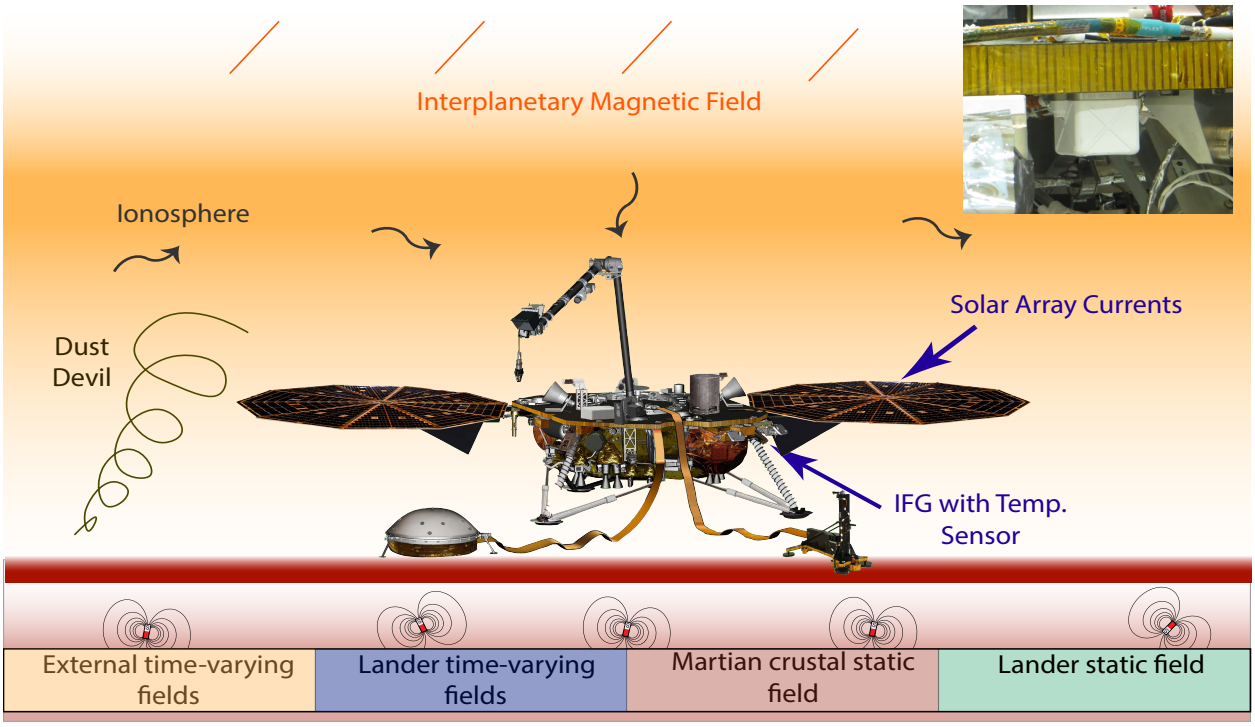
Interplanetary Magnetic Field
Ionosphere
Dust
Devil
Solar Array Currents
IFG with Temp.
Sensor
External time-varying fields
Lander time-varying fields
Martian crustal static field
Lander static field

Figure 4.

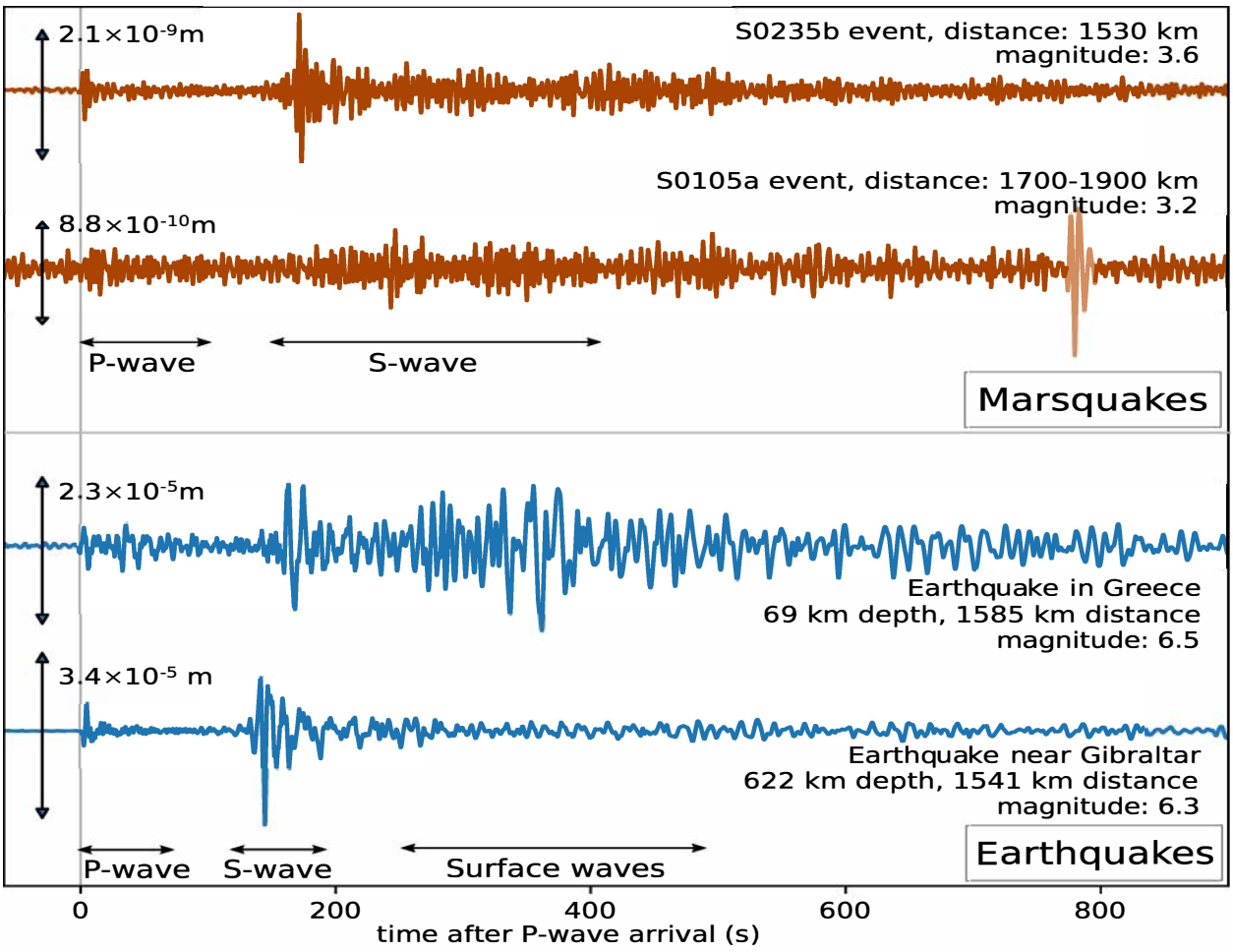
2.1×10-9m
S0235b event, distance: 1530 km
magnitude: 3.6
S0105a event, distance: 1700-1900 km
magnitude: 3.2
8.8×10-10m
P-wave
S-wave
Marsquakes
2.3×10-5m
Earthquake in Greece
69 km depth, 1585 km distance
magnitude: 6.5
3.4×10-5 m
Earthquake near Gibraltar
622 km depth, 1541 km distance
magnitude: 6.3
P-wave
S-wave
Surface waves
Earthquakes
0
200
400
600
800
time after P-wave arrival (s)

Figure 5.

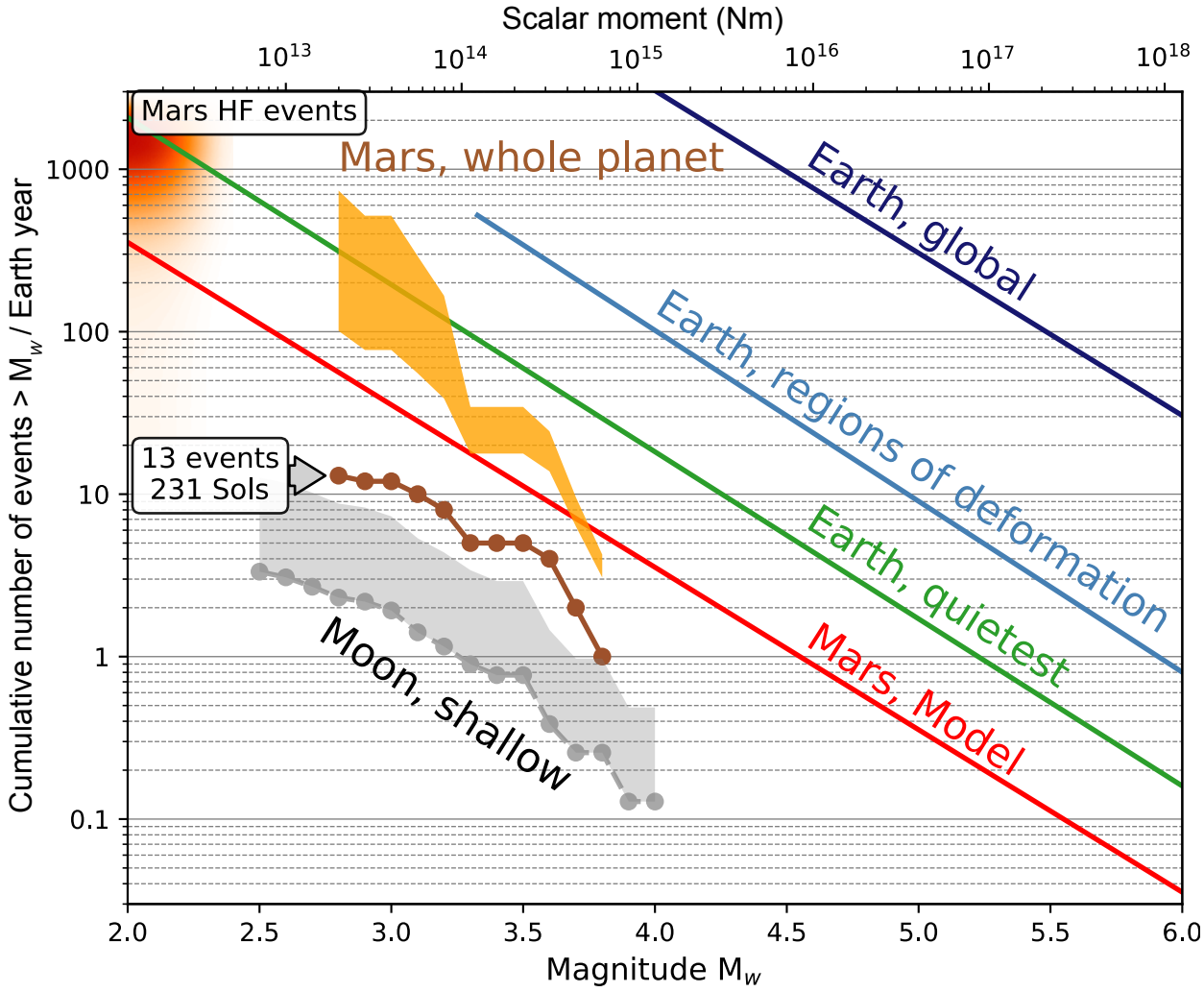
Scalar moment (Nm)
10^{13}
10^{14}
10^{15}
10^{16}
10^{17}
10^{18}
Mars HF events
Mars, whole planet
Earth, global
Earth, regions of deformation
Earth, quietest
Mars, Model
13 events
231 Sols
Moon, shallow
Cumulative number of events > M_w / Earth year
1000
100
10
1
0.1
2.0
2.5
3.0
3.5
4.0
4.5
5.0
5.5
6.0
Magnitude M_w

Box Figure.

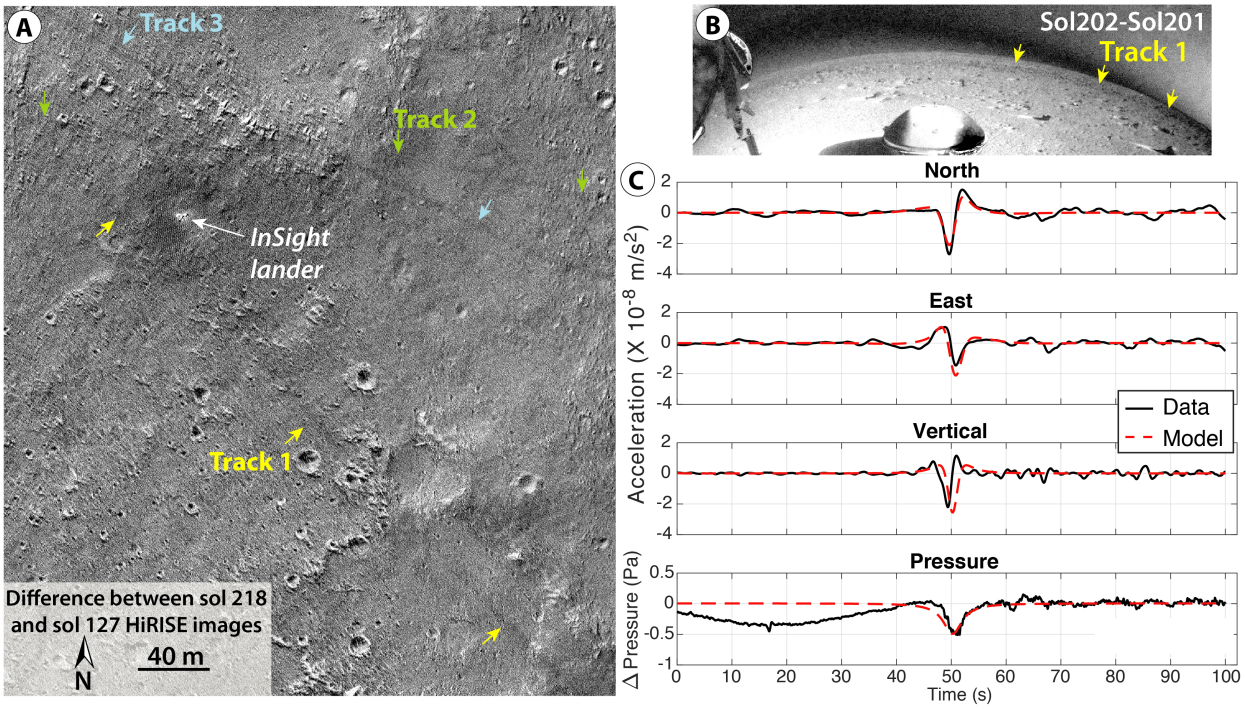
A
Track 3
Track 2
InSight
lander
Track 1
Difference between sol 218
and sol 127 HiRISE images
40 m
N
B
Sol202-Sol201
Track 1
C
North
East
Vertical
Pressure
Data
Model
Acceleration (X 10-8 m/s2)
ΔPressure (Pa)
Time (s)

Extended Data Figures

Extended Data Figure 1. Instrument Payload.

Instrument	Measurement
SEIS (Seismic Experiment for Interior Structure)[8]	Very-Broad-Band and Short-Period Seismometers – three-components of ground motion, 0.01–100 Hz, noise floor down to $\sim 10^{-10}$ m/s^2/Hz$^{1/2}$
HP^3(Heat Flow and Physical Properties Package)[9]	Mole and Science Tether – thermal gradient, thermal conductivity and mechanical properties in upper 5 m of regolith
	RAD (Infrared Radiometer) – ground surface temperature
RISE (Rotation and Interior Structure Experiment)[10]	X-Band Transponder – variations in planet rotation vector (direction and magnitude)
APSS (Auxiliary Payload Sensor Suite) [25]	TWINS (Temperature and Wind for InSight) – air temperature and wind direction and speed
	Pressure Sensor – atmospheric pressure
	IFG (InSight Fluxgate) – vector magnetic field
IDS (Instrument Deployment System) [49;50]	IDA (Instrument Deployment Arm) – ground mechanical properties
	IDC (Instrument Deployment Camera) – medium-resolution (FOV 45°) color camera (pointable)
	ICC (Instrument Context Camera) – wide-angle (FOV 120°) color camera (fixed)
LaRRI (Laser Retro Reflector for InSight)[51]	Passive retro-reflector array to support future precision laser ranging from Mars orbit

Extended Data Figure 2. Probability of marsquake detection.

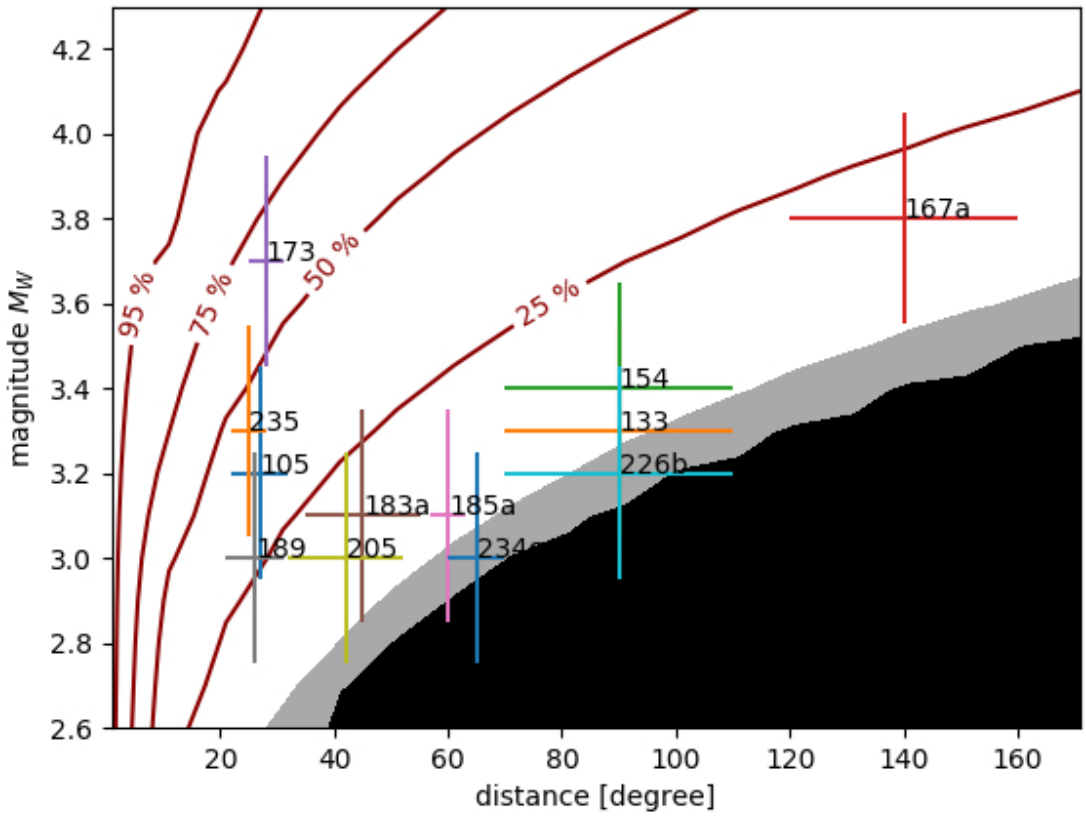

Probability to detect a marsquake of a certain distance and magnitude, given the expected source spectrum[2] and the distribution of ambient noise over sols 85-325. The colored crosses mark the 13 events described in the main article with their uncertainties in distance and magnitude M_w; numerical labels refer to event names in Giardini et al.[2] (e.g., 167a corresponds to S0167a). The black region is where the event would have never surpassed the ambient noise, the grey region is where it would have been observable only 10% of the time.

Extended Data Figure 3. Correction of numbers of events for variable noise across observation window. Events with magnitude M_w=2.8 are counted 4 times, events with M_w=3.8 are counted 2 times, with linear interpolation in between. Distances and magnitudes are based on waveform alignment and the spectral magnitude $M_{\mathrm{FB}}^{\mathrm{Ma}}$ (see Giardini et al.[2] for a full discussion of marsquake magnitudes).

Event	Distance (deg.)	M_W	n_i
S0105a	27 (±5)	3.2	3.2
S0133a	90 (±20)	3.2	3.2
S0154a	90 (±20)	3.5	2.6
S0167a	150 (±20)	3.8	2
S0173a	28 (±3)	3.6	2.4
S0183a	47 (±10)	3.1	3.4
S0185a	60 (±3)	3.1	3.4
S0189a	27 (±5)	3.0	3.6
S0205a	45 (±10)	3.0	3.6
S0226b	90 (±20)	3.2	3.2
S0234c	65 (±5)	2.8	4
S0235b	25 (±3)	3.6	2.4
S0325a	25 (±5)	3.7	2.2
Total number			39

Extended Data Figure 4. Minimum detectable magnitude for different distances, with the corresponding fractional surface of the planet.

Distance (degrees)	M_{min}	Fraction of the planet's surface
25	2.6	0.07
45	2.9	0.15
60	3.0	0.25
90	3.2	0.5
150	3.5	0.93

Extended Data Figure 5. Corrected distribution of events with magnitude.

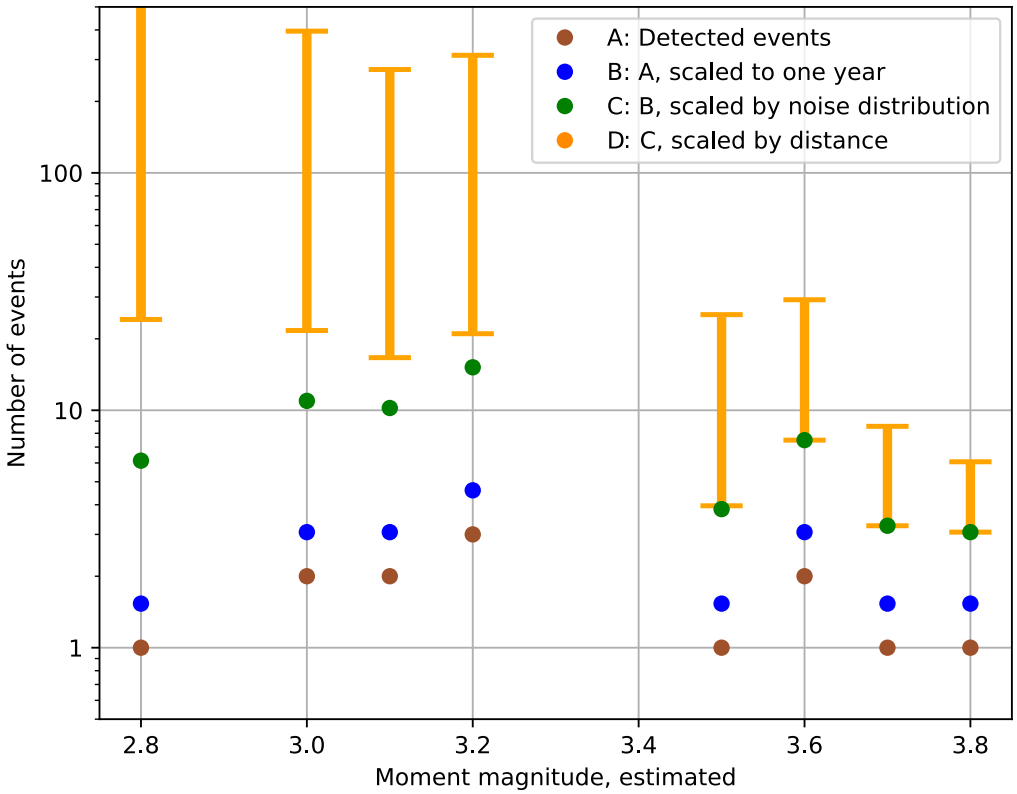

Distribution of events across magnitude, with the corrections described in the text.

Initial results from the InSight mission on Mars: Supplementary Discussion

Inversion of the shallow surface structure at the InSight landing site from multi-instrument observations of dust devils

In daytime, the intense turbulence in the lower atmosphere of Mars gives rise to frequent convective vortices, detected as pressure drops as well as associated wind and temperature signatures[1]. If enough dust is lifted from the surface by the convective vortex, a dust devil is formed. Before InSight, numerous dust devils were observed on Mars by in-situ and orbital cameras. Dust devils are known to generate tracks detected by orbital or surface imaging[2,3], and ground deformation as observed by seismic instrumentation[4]. Joint observation using multiple instruments provides the possibility of a complete description of the vortex event, including a temporal reconstruction of the dust devil event and the formation of associated tracks.

Since InSight landed in Elysium Planitia on 26 November 2018, multiple HiRISE images (25-cm spatial resolution[5]) have been acquired over the landing site. They allow the detection of the surface expression of multiple atmospheric processes, including vortex activity[6]. Seven HiRISE images of the area around InSight were acquired over the first eight months since landing, representing almost one orbital image per month. ICC images are taken on a daily basis, while SEIS and APSS operate continuously, with 20 sps acquisition for seismic and pressure data.

Since the beginning of the mission, many dust devil/convective vortex signatures have been detected by SEIS[7] and APSS[6], making Elysium Planitia one of the most active landing sites on Mars. However, no dust devils have been directly imaged so far by the ICC or IDC cameras[8].

Here we describe the first joint observations of a vortex event on a planetary surface made by orbital imaging and in-situ instrumentation (cameras, pressure and wind sensors, seismometer). These combined measurements offer the possibility to better understand atmospheric processes and investigate subsurface structure beneath the surface vortex track.

I. Description of the vortex signature on the various instruments:

I.a. Satellite and ICC images

After 8 months of monitoring, a dust devil track was identified in both in-situ ICC and orbital HiRISE images in the close vicinity of the InSight lander. On the HiRISE images, the closest track is situated SW of the lander, trending $\sim$ N136° E, at a distance of $\sim$ 19 m from SEIS at its closest approach (track 1 in Figure S-1A). The track, and therefore the vortex, is at least $\sim$ 5-7 m wide. These measurements are all confirmed by the

semi-autonomous track detection we performed (Figure S-1B). Note that we also observe two tracks in the north, trending N100° E to N115° E, at 41 m and 65 m from SEIS, respectively (tracks 2 and 3 in Figure S-1A). This is the first time that clear dust devil tracks have been observed at a distance <50 m from SEIS on HiRISE images (see Figure S2-5 in Lognonné et al.[7]). On the basis of these HiRISE images, we are able to pinpoint the date of these new track appearances to within a three-month time interval, between April 6 (sol 127) and July 8 (sol 218).

Towards the end of this interval a dust devil track was also detected in ICC images (Figure S1-2). As they are acquired on a daily basis, ICC images place strong constraints on the date of occurrence. While the track is not observed between sols 203 and 217 (Figure S-2A), it is clearly detectable between sols 199 and 202 (Figure S-2C). The track clearly shows up in the sol 202-201 difference images (Figure S-2D), but not in sol 200-199 and sol 201-200 difference images (Figures S-2E and S-2F). Surprisingly, we can also barely distinguish a track on sol 206-203 difference images (Figure S-2B) at the exact same location, while no tracks appear on difference images spaced by a longer period of time (Figure S-2A). Since it is unlikely that a new track overlaid the previous one with the same azimuth and distance from the lander, we consider that the sol 206-203 track is the same track as the sol 202-201 track. We suggest that the track might have been further modified by surface processes (e.g., possible slight dust removal and darkening of the newly formed track by ambient wind). To summarize, ICC images imply that the dust devil track formed between the ICC image acquisition times of sol 201 (5:22pm LMST, Local Mean Solar Time) and sol 202 (4:41pm LMST). The ICC images situate the track from about 20-22 m from the ICC camera in the SW direction (thus about 19-21 m from SEIS) to 35-40 m out in the S to SSW direction.

The similarity between our observations on satellite and ground images leads us to conclude that HiRISE and ICC captured the same dust devil (track 1). We can thus infer that the distance and azimuth estimated from HiRISE describe a track which formed between sol 201 and sol 202. The restricted time interval (sol 201 5:22pm LMST to sol 202 4:41pm LMST), distance (19 ± 1 m), minimum width (5 to 7 m) and azimuth (N136° E) of dust devil track 1 will be used in the following sections.

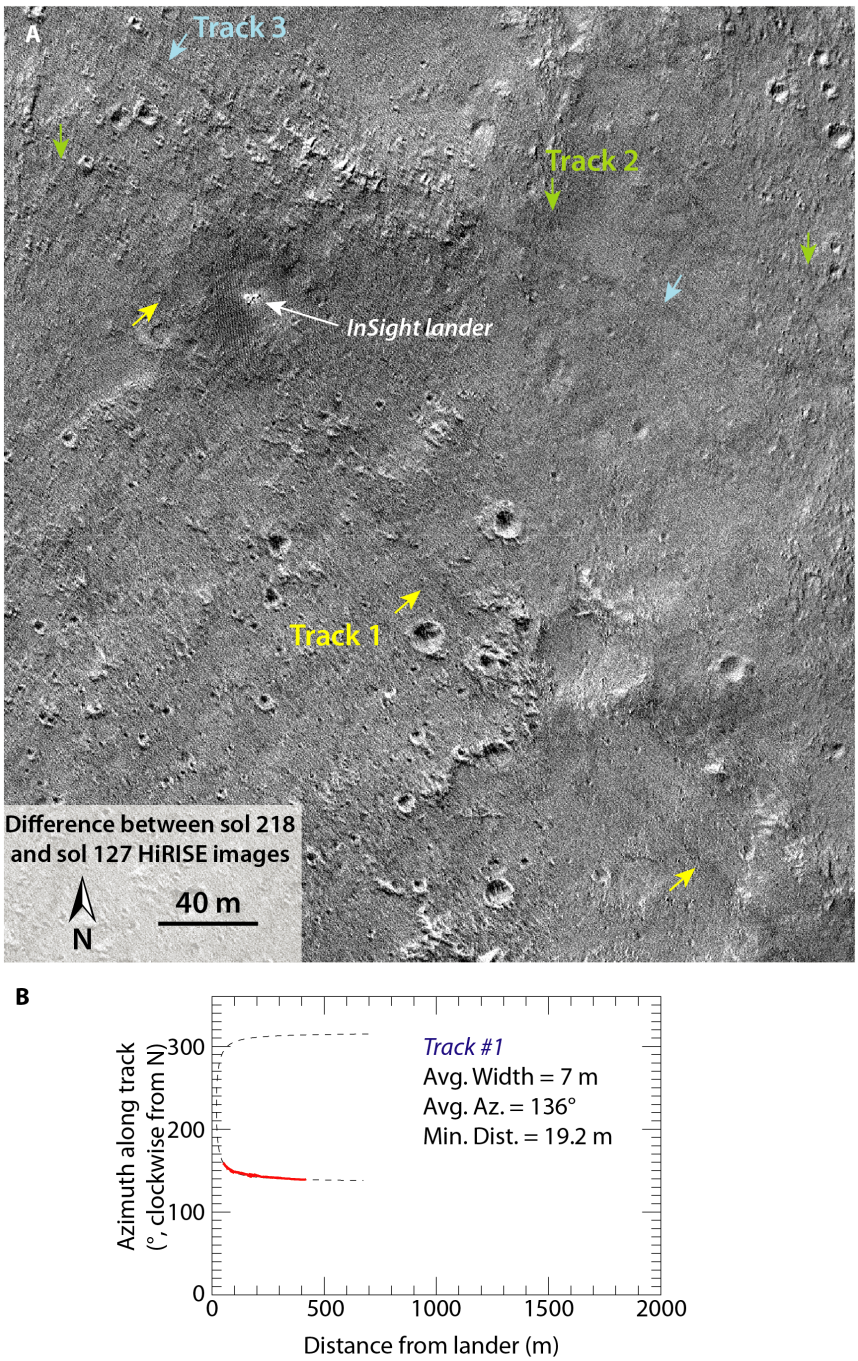

Figure S-1: (A) Difference between HiRISE images ESP060695_1845_RED (July 8, 2019; sol 218) and ESP059495_1845_RED (April 6, 2019; sol 127) showing new dust devil tracks (dark traces) near the InSight lander. The three main tracks have been highlighted by colored arrows. (B) Azimuth as a function of distance from the Insight lander along track 1, determined from semi-autonomous track detection using the radon transform technique[9]. Red and dotted lines are clear detection and inferred detection of the track, respectively, assuming that the track is a linear feature.

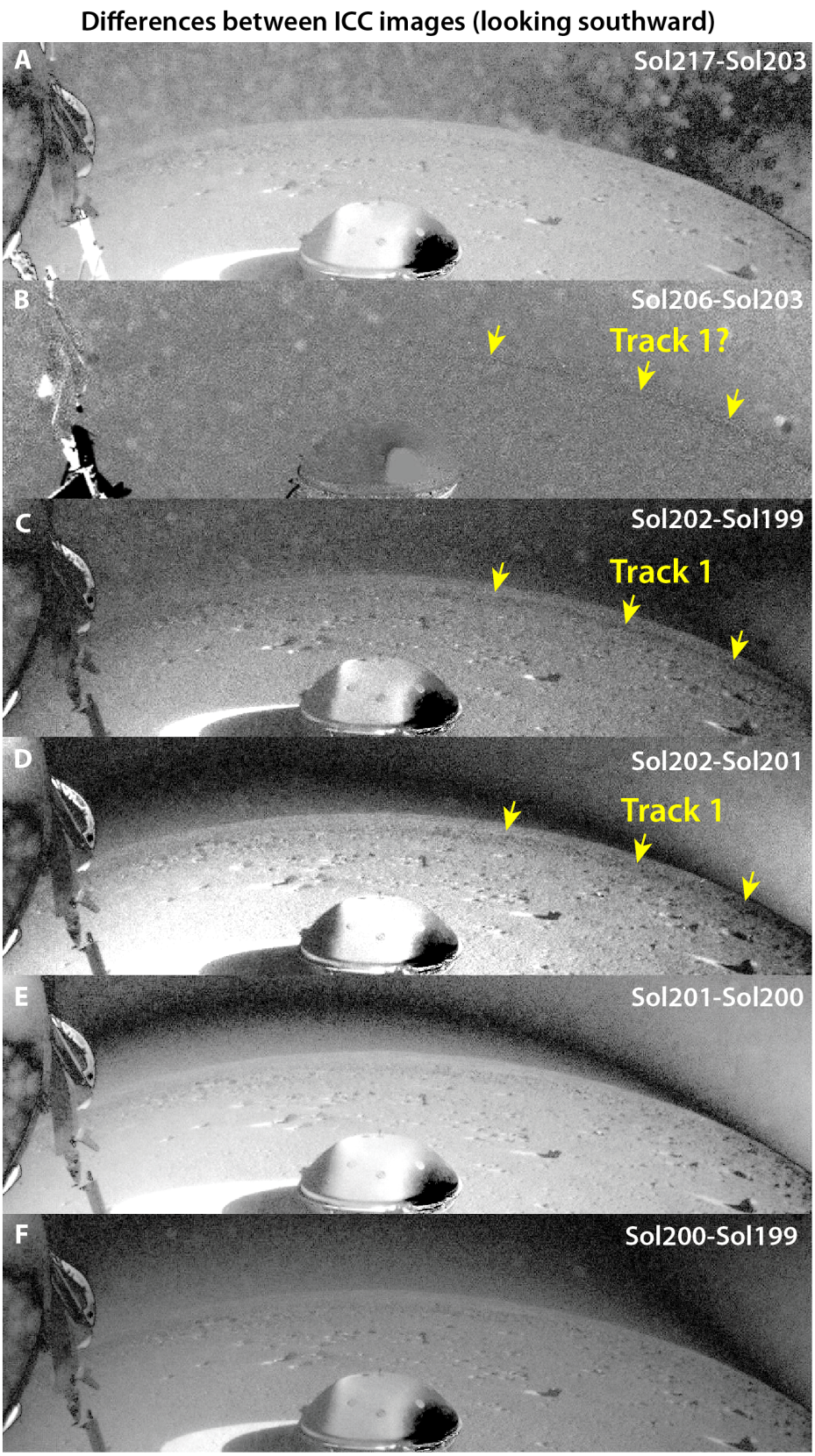

Figure S-2: Differences between ICC images taken on different sols. A faint dark dust devil trace is highlighted by yellow arrows on the sol 206-sol 203, sol 202-sol 199 and sol 202-sol 201 difference images (B, C and D, respectively), and is not observed on the sol 217-sol 203, sol 201-sol 200 and sol 200-sol 199 difference images (A, E and F, respectively).

I.b. SEIS and APSS data

Since the beginning of the InSight mission, vortices detected by their associated pressure drop are particularly active during the day (especially between 11 am and 3 pm LTST[6], Local True Solar Time) and stop at the end of afternoon ($\sim$ 5 pm LMST). This implies that the convective vortex responsible for this track likely occurred on sol 202, and not 201, since the ICC image that pre-dates the event was taken on sol 201 at 5:22 pm LMST. According to the pressure-drop detection algorithm[6], 34 pressure drops >0.3 Pa occurred on sol 202 at the InSight landing site between about 8 am and 4 pm LMST.

As described above, orbital data allow the mean track direction to be constrained; as the vortices are transported by the wind, the direction of the track trace is also the most likely ambient wind direction. Wind data from TWINS confirm this as the dominant daytime wind direction ($\sim$ N140° E, i.e. blowing from SE to NW). Ambient wind speeds ranged from 5 to 11 m/s during the turbulent daytime period of sol 202 (Figure S-3). Altogether, this information corroborates that the convective vortex passed to the SW of SEIS at its closest approach.

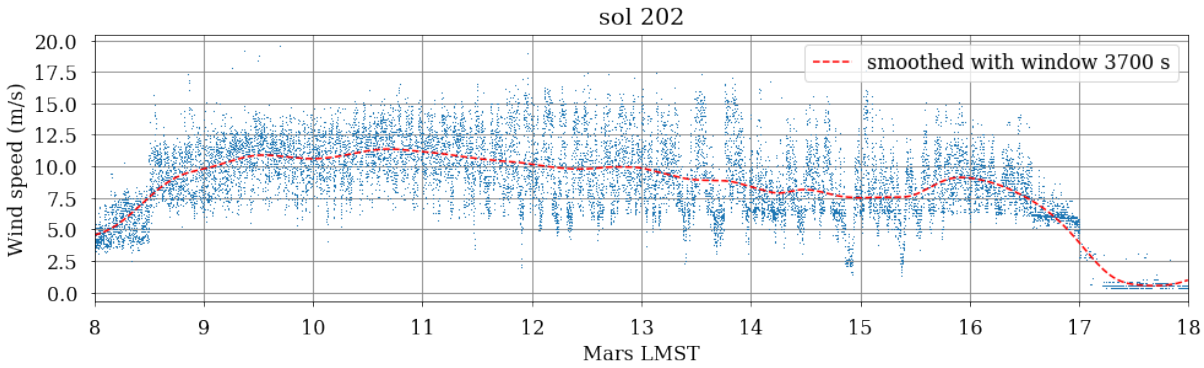

Figure S-3: Wind speed data (blue) and averaged data over a moving window 1h long (red) for the daytime period of sol 202.

In order to select candidate events in the InSight data, the seismic measurements are vital: the ground will deform and tilt as the vortex passes by. An analysis of the source azimuth from the seismic data for each of the 34 pressure drops detected on sol 202 allows events with a close approach in the SW direction to be identified (Figure S-4). To further constrain the list of candidate events we generate a model prediction of the SEIS and APSS measurements of the convective vortex along the predefined track (N136° E; Figure S-5a) based on previous models[4,10]. This is used to identify the events with the correct waveforms (not amplitudes). From this process one event on sol 202 at 7:59 Coordinated Universal Time (UTC) (13:10 LMST) is a clear candidate displaying both the correct azimuth (Figure. S-4) and waveform (Figure S-5b). Several methods have been used to determine the azimuth of the potential candidates, such as polarization of the dust devil signals to retrieve the back-azimuth[11]. We obtain similar results for the best candidate, showing a first arrival coming from the southeast ($\sim$ N160° E), which then switches toward the north. We note that this candidate event is not one of the biggest pressure drops on sol 202. The largest pressure drops did not have a closest approach azimuth to the SW.

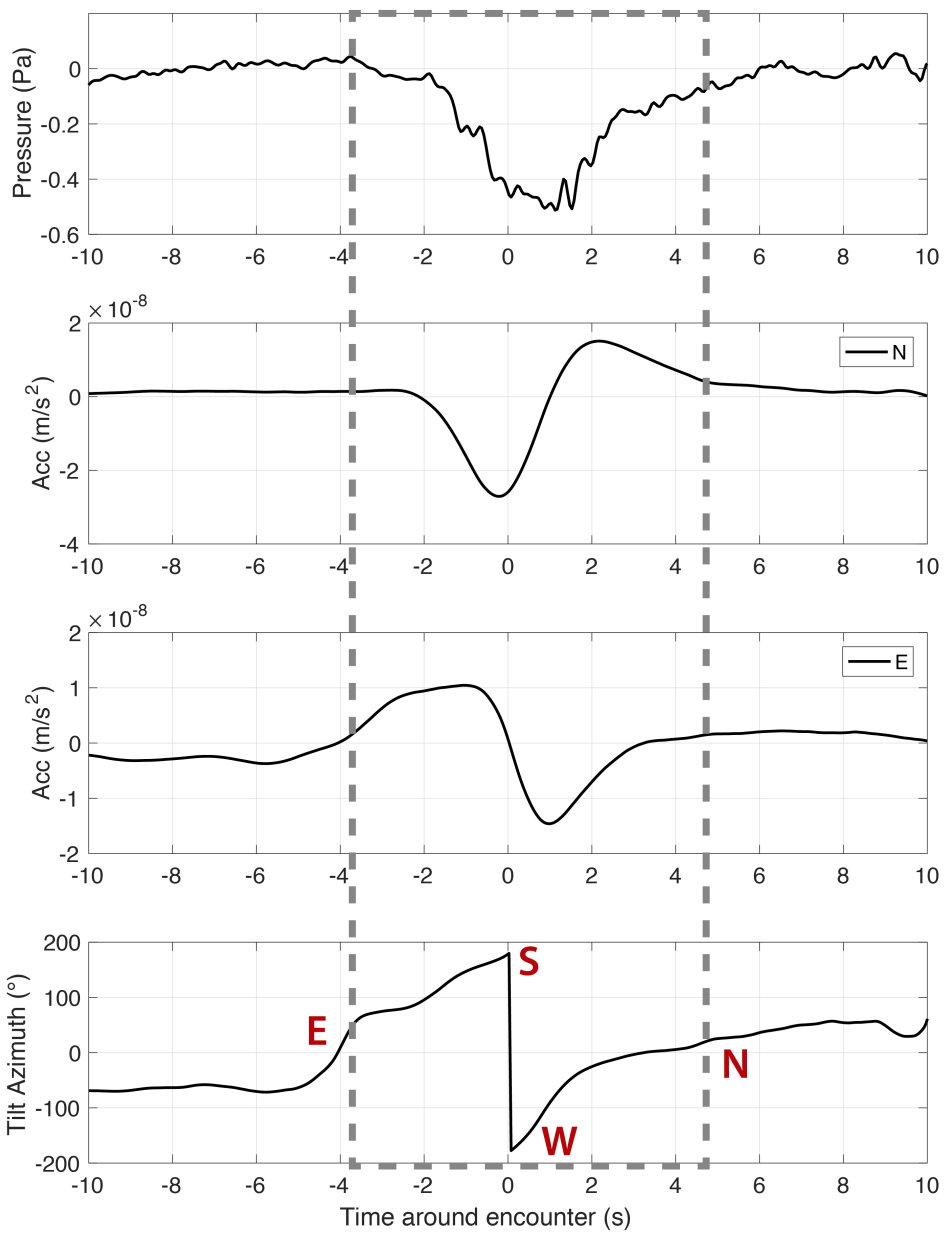

Figure S-4: Observed pressure and seismic (horizontal, N and E) data for the event at 7:59 UTC (13:10 LMST) on sol 202. The azimuth (lower figure) during the event (grey dashed box) varies from E at the start of the encounter to S then W, before pointing N. The closest approach (when the pressure signal is largest in amplitude) occurs to the SW of SEIS.

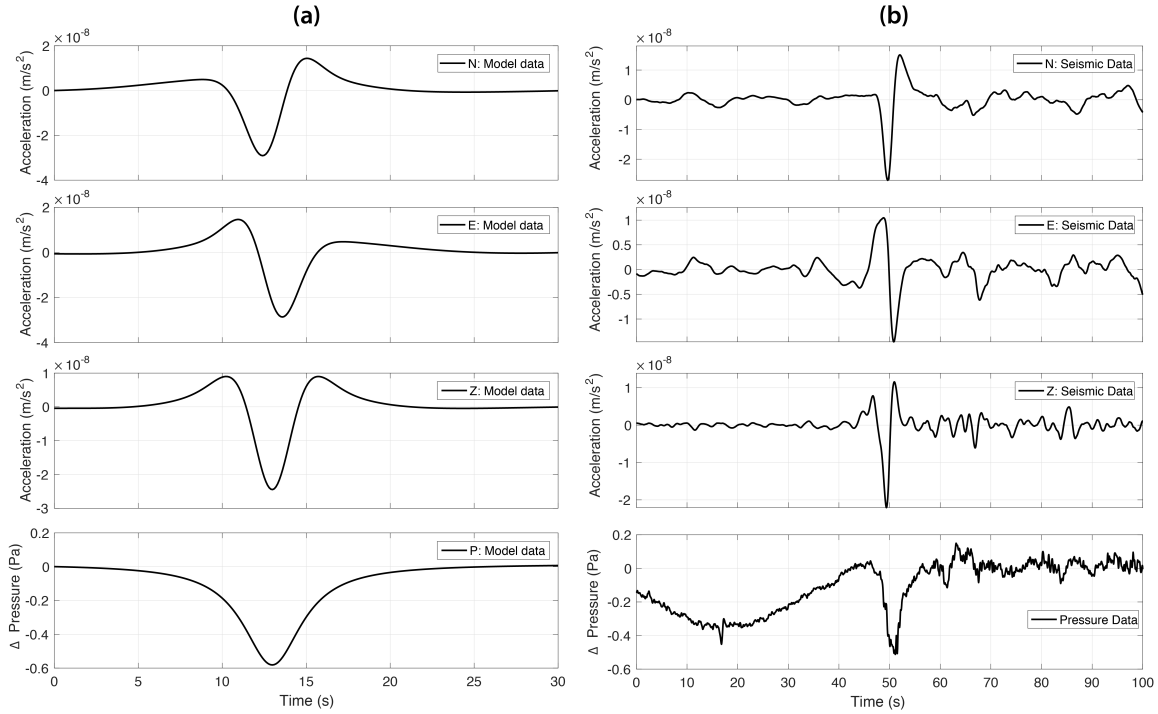

Figure S-5: (a) Synthetic waveforms for the expected pressure and seismic data for the track 1 trajectory. (b) The observed pressure and seismic data for the event at 7:59 UTC (13:10 LMST) on sol 202.

The wind speed and direction data for this event are shown in Figure S-6. There is no obvious signature of the vortex rotation in the wind direction data, indicating that this vortex probably did not pass directly over InSight. There is only a moderate increase in the wind speed at the time of the event further suggesting that we are only detecting the edge of the vortex at the InSight lander. At the time of this event (13:10 LMST), the ambient background wind was $\sim$ 9.5 m/s (Figure S-3).

From the above analyses we can compile a list of known vortex parameters for the event on sol 202 at 7:59 UTC (13:10 LMST). This list (Table S-1) can then be used to fit the observed data and constrain the vortex pressure distribution model and ground parameters at the InSight landing site.

Vortex Parameter	**Value**	**Method of Determination**
Trajectory	N136° E	HiRISE images
Closest approach distance	19 m	HiRISE + ICC images
Advection speed	$\sim$ 9.5 m/s	TWINS
Advection direction	From SE to NW	TWINS + HiRISE
Vortex diameter	$>$5 m, $<$ 19 m	HiRISE images + PS
Vortex core pressure	$<$ 9 Pa	PS (statistics)

Table S-1: Constraints on vortex parameters from the combined multi-instrument measurements.

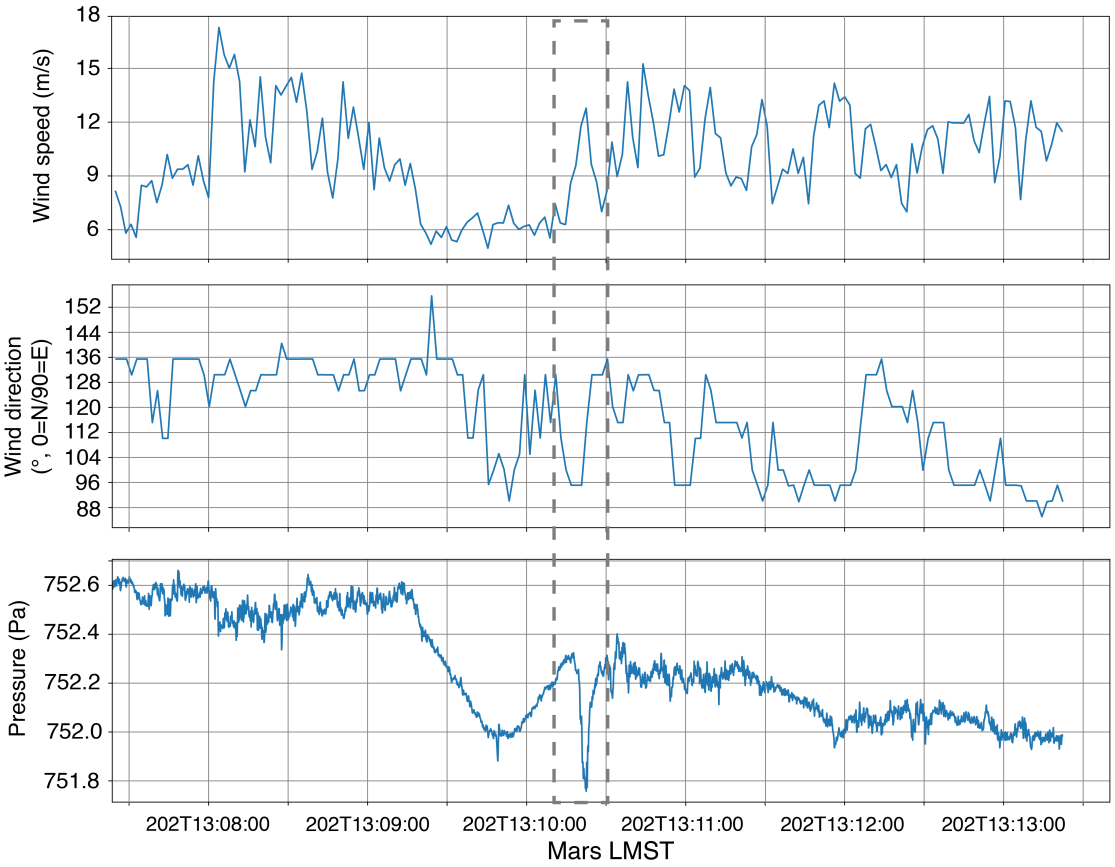

Figure S-6: Pressure (bottom), along with wind speed (top) and direction (middle) data at the time (in LMST) of the vortex passage (indicated by the grey dashed box). The wind direction is that from which the wind blows, indicated clockwise from north.

II. Constraints on vortex models and the Martian sub-surface

II.a. Constraints on vortex parameters and pressure distribution models

Several models exist to describe the variation of the pressure from the centre of a vortex[4,12,13]. In addition, as the total negative load of a vortex is the integral of the pressure over the vortex diameter, the pressure distribution has important implications for studies of ground deformation due to vortices[4,14]. Here, as we know precisely the trajectory of the vortex, we have a unique opportunity to study how the pressure varies with distance from the vortex centre.

Assuming the trajectory, closest approach distance and advection speed described in Table S-1, we generate synthetic pressure and seismic time series that would be observed by InSight for each pressure distribution model and each combination of vortex parameters (see example in Figure S-5a; parameters for this case are: closest approach distance = 19 m, advection speed = 9.5 m/s, core pressure drop = 5.5 Pa, convective vortex diameter = 6 m and Young's modulus = 2.7x10^8 Pa). We then calculate the residual between the

synthetic model and the observed pressure data during 20 s around the vortex encounter in order to determine the possible range of vortex parameters for this particular event. The combinations of vortex radii and core pressure drops that produce the pressure drop observed by InSight (0.48 Pa; Figure S-4) are shown in Figure S-7 for each pressure distribution model.

Considering the absolute values of the residuals, the Lorenz et al.[4] (L) method appears to be a better fit to the data. However, solutions with similar minimum residuals are found for all three models. Given the distribution of observed pressure drops since InSight landed on Mars[6], the parameter range solutions for the Ellehoj et al.[13] (E) and Vatistas et al.[12] (V) models are perhaps more reasonable.

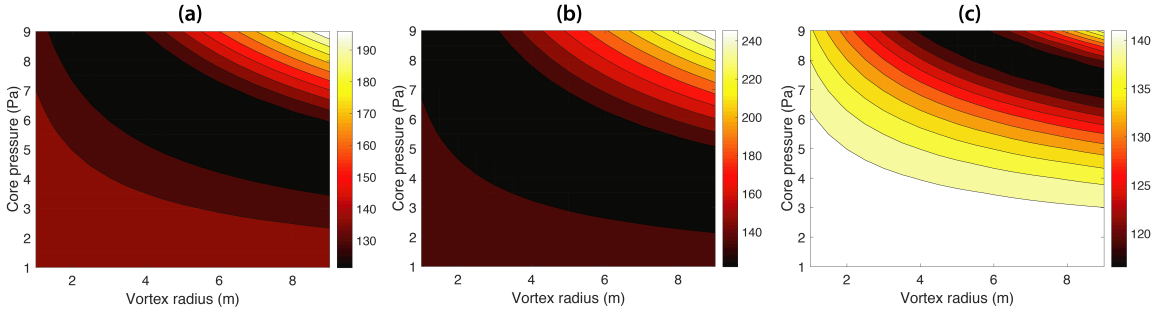

Figure S-7: Contour plots showing the parameter space considered for the different pressure variation models: (a) V, (b) E and (c) L. The colour represents the total absolute residual between the observed pressure and the synthetic data over a period of 60 s around the encounter, with the darkest colour showing the best fitting properties.

Combining these solutions for the pressure data with a similar analysis for the three components of the seismic data allows us to further constrain the possible vortex properties. Figure S-8a shows vortex parameters capable of reproducing the observed seismic signal on the three components (dark regions) when the E model is used. Here we assume the mean Young's modulus of the martian ground derived for this event (see Section II c), which is in good agreement with the estimations made from a collection of 360 vortex signals[7]. The best fitting regions for the four observables can be compared (Figure S-8b) to identify the most probable vortex parameters. For the E model, the four regions do not overlap simultaneously, but the most probable vortex parameters are likely close to the region between the upper red line and the upper green line. The V model results are almost identical to the E model results. In comparison, the region of near overlap in the L model is very small and requires a very large core pressure (>8 Pa). From this we can conclude that the E or V models are probably more representative of the vortex pressure distribution on Mars. In addition, if these models are more physically correct, this implies that the ground compliance does not vary with distance (Figure S-9), as suggested by the accumulated observations[7], an important validation for the methods applied to retrieve the ground compliance in Section II b.

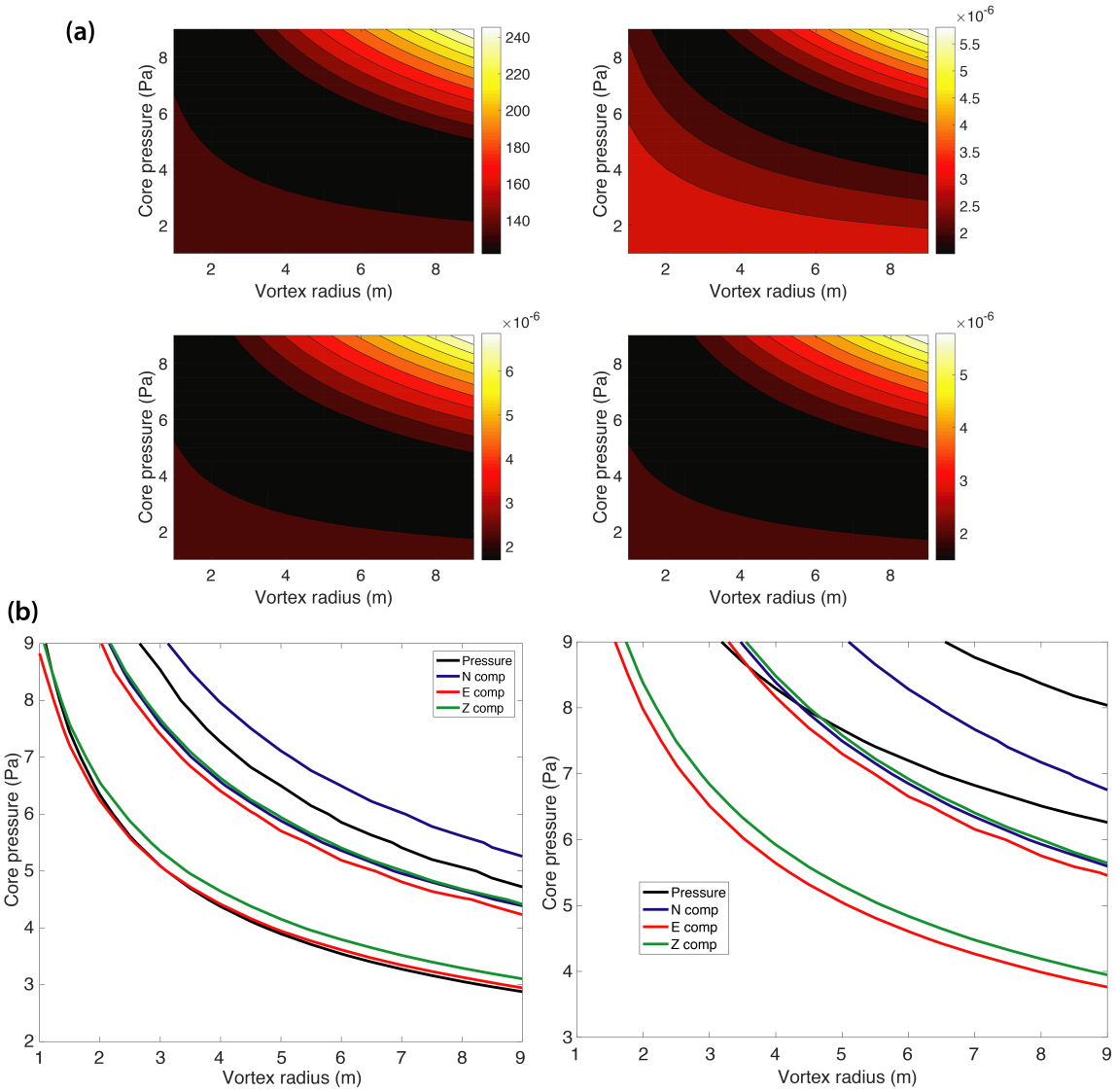

Figure S-8: (a) Contour plots showing the total absolute residual between the observed pressure (top left) and seismic data (N: top right, E: lower left, Z: lower right), and the synthetic data over a period of 60 s around the encounter. The E pressure model is used here. The darkest colour shows the best fitting parameter combinations. (b) The regions with the best fitting solutions for each of the data sets for the E model (left) and the L model (right). The best fitting pressure solutions fall between the black lines, and the best fitting N, E and Z seismic solutions fall between the blue, red and green lines, respectively. For these analyses we assume a Young's modulus of 270 MPa and a Poisson's ratio of 0.22 (see Section II b).

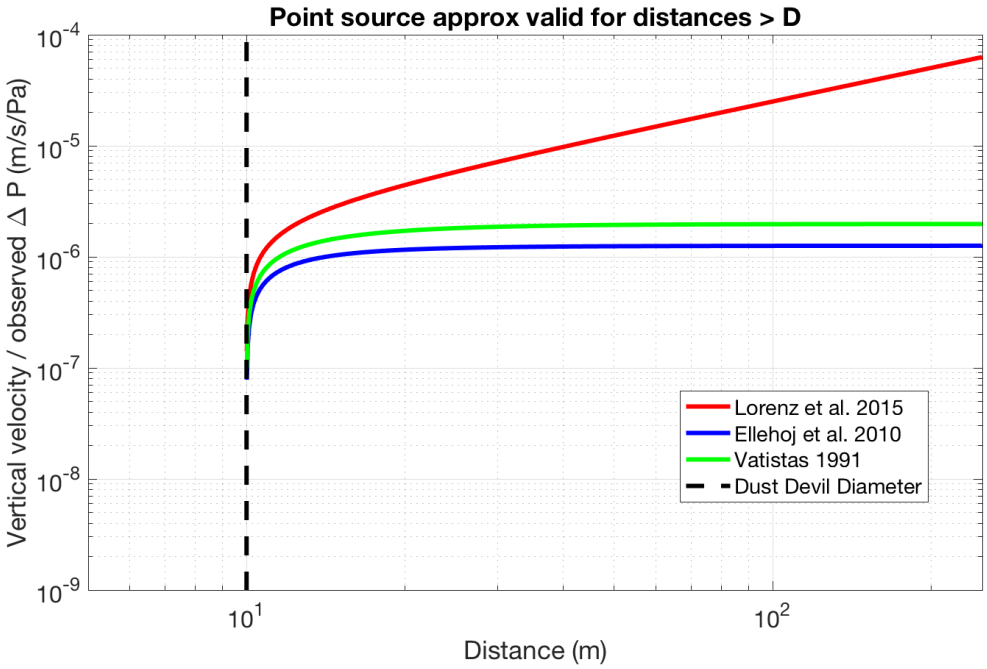

Figure S-9: Pressure dependence as a function of distance for different models

II.b. Ground compliance

In the vertical direction, the quasi-static ground motion can be modelled based on the pressure and wind time series and the frequency-dependent ground compliance (the ratio between vertical velocity and pressure forcing). The frequency dependence is related to the sensitivity of elastic properties with depth, which scales with frequency. We use this theory[14,15], which was applied to InSight seismic and meteorological data for about 360 vortices[7], to measure the compliance of the sol 202 event as a function of frequency. In contrast to the multiple-measurements technique[7], we can pinpoint the location of compliance sounding at the closest approach of the dust devil with respect to SEIS.

The compliance is calculated in the frequency band 0.03 to 0.3 Hz where the coherence between the pressure and the seismic signal is the largest, and is normalized by the averaged wind of 9.5 m/s . The mean compliance in this bandwidth is 7×10^{-9} Pa^{-1}, which corresponds to a mean Young's modulus of 270 MPa. The compliance values (Figure S-10b) show a clear increase with frequency that is consistent with an increasing Young's modulus with depth.

The compliance measurements allow us to provide constraints on the subsurface model to the W/SW of SEIS beneath the dust devil track. The inverse problem consists of retrieving both the Young's modulus and Poisson's ratio in the first 20 m below the surface from compliance data. However, the problem is underdetermined in the sense that different subsurface models can lead to similar misfit values. In order to go beyond the classical computation of the unique best-misfit solution model, and to provide a quantitative measure of the model uncertainty and non-uniqueness, a Markov chain Monte Carlo algorithm is used[16–18]. This provides robust probability density functions (PDFs) of the

elastic parameters as a function of depth. The forward problem is based on the Sorrells theory[15], which links the elastic properties to the compliance as a function of frequency. The depth of the regolith/bedrock interface is randomly sampled, as well as the Young's modulus and the Poisson's ratio in the bedrock. The compaction of the regolith is assumed using an empirical power law (equations 1 and 20 of Morgan et al.[19]), assuming that the medium is densely compacted. We set the density of the bedrock to 2600 kg/m^3, which is about 15% less than typical basalts[19]. Density is not constrained and is used only for representing the result of the inversion of Young's modulus and Poisson's ratio in terms of seismic compressional wave velocity V_p.

The results are shown in Figure S-10a. All possible solutions of V_p profiles are represented, the non-uniqueness being due to trade-offs among the seismic velocities in the regolith and bedrock and the depth of the regolith/bedrock interface. The data fit (Figure S-10b) show that all the models accepted by the algorithm fit the compliance data within their uncertainty bounds. Compared to the previous model[7], where V_p in the regolith is constrained from the apparent velocity estimated from HP^3 hammering, the distribution shows higher seismic velocities for the uppermost few meters. It is, however, quite comparable to the seismic velocities obtained from the inversion of the collection of 360 vortices without the HP^3-SEIS apparent velocity constraint shown in Figure S2-6c2 of Lognonné et al[7].

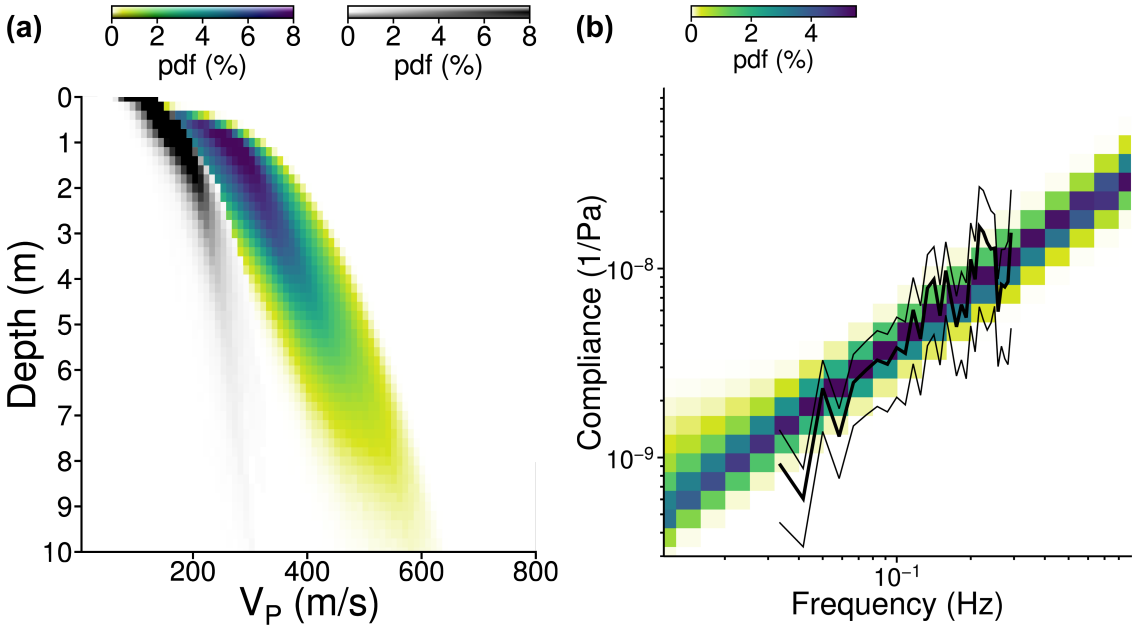

Figure S-10: (a) Comparison of the V_p probability density function (PDF) as a function of depth for 2 cases: (1) the PDF retrieved from the compliance of the convective vortex recorded on sol 202 (viridis colormap), and (2) the PDF constrained using the compliance values from 360 vortices between sol 72 and sol 168 and the apparent V_p estimated from HP^3 hammering[7] (gray scale). Yellow and blue colours are low and high probabilities, respectively. The PDFs are computed using 12,000 models. The PDF values are computed by counting the number of models in each 10 m/s V_p interval, every 0.1 m depth. For a given depth, the sum of the PDF over all the V_p intervals is equal to 100%. (b) Output probability distribution of the compliance as a function of frequency determined from the analysis of the convective vortex recorded on sol 202. The thick and thin black lines show the input compliance measurements and their uncertainties, respectively.

References

1. Spiga, A., et al., 2018. Atmospheric science with InSight. Space Science Rev., v. 214, p. 109, doi: 10.1007/s11214-018-0543-0.

2. Balme, M., and Greeley, R., 2006. Dust devils on Earth and Mars. Rev. Geophys., v. 44, p. RG3003, doi: 10.1029/2005RG000188.

3. Reiss, D., et al., 2016. Dust devil tracks. Space Science Rev., v. 203, p. 143–181, doi: 10.1007/s11214-016-0308-6.

4. Lorenz, R. D., et al., 2015. Seismometer detection of dust devil vortices by ground tilt. Bull. Seismol. Soc. Am., v. 105, p. 3015–3023, doi: 10.1785/0120150133.

5. McEwen, A.S., et al., 2007. Mars Reconnaissance Orbiter's High Resolution Imaging Science Experiment (HiRISE). J. Geophys. Res., v. 112, p. E05S02, doi: 10.1029/2005JE002605.

6. Banfield, D., and Spiga, A., et al., 2020. The atmosphere of Mars as observed by InSight. Nat. Geosci., submitted.

7. Lognonné, P., et al., 2020. Constraints on the shallow elastic and anelastic structure of Mars from InSight seismic data. Nat. Geosci., submitted.

8. Maki, J. N., et al., 2018. The color cameras on the InSight lander. Space Science Rev., v. 214, p. 105, doi: 10.1007/s11214-018-0536-z.

9. Toft, P., 1996. The Radon Transform - Theory and Implementation. PhD Thesis, Kgs. Lyngby, Denmark, Technical University of Denmark.

10. Murdoch, N., et al., 2017. Estimations of the seismic pressure noise on Mars determined from large eddy simulations and demonstration of pressure decorrelation techniques for the InSight mission. Space Science Rev., v. 211, p. 457–483, doi: 10.1007/s11214-017-0343-y.

11. Schimmel, M., Stutzmann, E., Ardhuin, F., and Gallart, J., 2011. Polarized Earth's ambient microseismic noise. Geochem., Geophys., Geosystems, v. 12, p. 14, doi: 10.1029/2011GC003661.

12. Vatistas, G. H., Kozel, V., and Mih, W. C., 1991. A simpler model for concentrated vortices. Exper. Fluids, v. 11, pp. 73–76, doi: 10.1007/BF00198434.

13. Ellehoj, M. D., et al., 2010. Convective vortices and dust devils at the Phoenix Mars mission landing site. J. Geophys. Res., v. 115, p. E00E16, doi: 10.1029/2009JE003413.

14. Kenda, B., et al., 2017. Modeling of ground deformation and shallow surface waves generated by martian dust devils and perspectives for near-surface structure inversion. Space Science Rev., v. 211, p. 501–524, doi: 10.1007/s11214-017-0378-0.

15. Sorrells, G. G., 1971. A preliminary investigation into the relationship between long-period seismic noise and local fluctuations in the atmospheric pressure field: Geophys. J. Int., v. 26, p. 71–82, doi: 10.1111/j.1365-246X.1971.tb03383.x.

16. Drilleau, M., et al., 2013. A Bayesian approach to infer radial models of temperature and anisotropy in the transition zone from surface wave dispersion curves. Geophys. J. Int., v. 195, p. 1165–1183, doi: 10.1093/gji/ggt284.

17. Panning, M. P., et al., 2015. Verifying single-station seismic approaches using Earth-based data: Preparation for data return from the InSight mission to Mars. Icarus, v. 248, p. 230–242,
doi: 10.1016/j.icarus.2014.10.035.

18. Panning, M. P., et al., 2017. Planned products of the Mars Structure Service for the InSight mission to Mars. Space Science Rev., v. 211, p. 611–650, doi: 10.1007/s11214-016-0317-5.

19. Morgan, P., et al., 2018. A pre-landing assessment of regolith properties at the InSight landing site. Space Science Rev., v. 214, p. 104, doi: 10.1007/s11214-018-0537-y.